

The Asian monsoon over the past 640,000 years and ice age terminations

Hai Cheng^{1,2}, R. Lawrence Edwards², Ashish Sinha³, Christoph Spötl⁴, Liang Yi⁵, Shitao Chen⁶, Megan Kelly², Gayatri Kathayat¹, Xianfeng Wang⁷, Xianglei Li¹, Xinggong Kong⁶, Yongjin Wang⁶, Youfeng Ning¹ & Haiwei Zhang¹

Oxygen isotope records from Chinese caves characterize changes in both the Asian monsoon and global climate. Here, using our new speleothem data, we extend the Chinese record to cover the full uranium/thorium dating range, that is, the past 640,000 years. The record's length and temporal precision allow us to test the idea that insolation changes caused by the Earth's precession drove the terminations of each of the last seven ice ages as well as the millennia-long intervals of reduced monsoon rainfall associated with each of the terminations. On the basis of our record's timing, the terminations are separated by four or five precession cycles, supporting the idea that the '100,000-year' ice age cycle is an average of discrete numbers of precession cycles. Furthermore, the suborbital component of monsoon rainfall variability exhibits power in both the precession and obliquity bands, and is nearly in anti-phase with summer boreal insolation. These observations indicate that insolation, in part, sets the pace of the occurrence of millennial-scale events, including those associated with terminations and 'unfinished terminations'.

The seasonal cycle of solar heating over Asia gives rise to the Asian monsoon (AM), a vast system of overturning atmospheric circulation that transports heat and moisture during boreal summer across the Indian Ocean and the tropical western Pacific into the Indian subcontinent and southeastern Asia, and as far as northern China and Japan¹ (Extended Data Fig. 1). Cave climate records have been important in characterizing AM changes and their causes. Such records demonstrate large and, in many cases, abrupt changes in monsoon intensity, inferred to have affected large swaths of Asia^{1–4}. A hallmark of these records is the precision with which age can be determined with modern U–Th dating methods⁵, thus allowing direct comparison with the orbital cycles without requiring orbital tuning^{1–4}. This approach, however, has been hindered by limited temporal coverage. Here we report a record from China, which, together with previously published data, covers the complete U–Th dating range from 640,000 years (640 kyr) ago to the present. Previous Chinese cave studies have demonstrated a close correspondence between changes in the AM and shifts in Northern Hemisphere summer insolation (NHSI) on orbital timescales^{3,6} and a close relationship between the AM and climate in the North Atlantic region on millennial scales^{1–4,7,8}. The latter has been used to correlate monsoon records with records from the North Atlantic region^{1–4,8}. Of note are Heinrich stadials (HSs) or ice rafted debris (IRD) events of North Atlantic origin, some of which coincide with Weak Monsoon Intervals (WMIs) in China^{4,8}. This correlation has been used to transfer the cave chronology to the marine oxygen isotope record, a strategy that has been important in establishing the timing of ice age terminations⁴ and which we apply here.

Our new $\delta^{18}\text{O}$ data from Sanbao Cave, China, allow us to establish the timing of Terminations (T) V through to VII in addition to the previously determined timing of terminations back to T-IV (ref. 4). First, this allows us to test ideas about the 100-kyr pacing of late Pleistocene ice age cycles⁹ and the degree to which termination timing is consistent with obliquity and/or precession forcing^{10–16}. Second, after removing the component of the AM that correlates with insolation, we examine

the residual suborbital variation⁸ over the full record. We show that some aspects of millennial-scale variability relate to orbital geometry. Third, the full record now crosses the Mid-Brunhes Event (MBE), when the character of CO₂ and ice volume cycles changed^{17–20}. We assess the degree to which these changes affected the AM. Fourth, we estimate the timing and duration of maximal AM strength over the Marine Isotope Stage (MIS) 11, a period of time which can be used as an analogue to the Holocene and future climate because of similar orbital geometry²¹.

Samples and results

Sanbao Cave is on the northern slope of Mt Shennongjia in central China (110° 26' E, 31° 40' N, elevation 1,900 metres above sea level). Mean annual temperature is 8 °C, and mean annual precipitation is 1,950 mm, 80% of which occurs during the summer (June to August). Four new stalagmites were collected ~1,500 m from the cave entrance. Samples were dated by a recently improved ²³⁰Th dating technique⁵, yielding precise age control (for example, ±1.5 kyr at the time of T-V) (Extended Data Figs 2, 3 and Supplementary Table 1). New $\delta^{18}\text{O}$ measurements have a temporal resolution of between 200 and 70 years (average of ~120 years) (Extended Data Fig. 4 and Supplementary Table 1). The replication test (Extended Data Figs 2, 4) and other lines of reasoning^{1–4} suggest that speleothem $\delta^{18}\text{O}$ variability results from changes in the $\delta^{18}\text{O}$ of precipitation.

The climate interpretation of changes in the cave $\delta^{18}\text{O}$ records from China remains a subject of intense debate¹. However, most studies support one or both of the ideas presented in the original studies. Yuan *et al.*²² invoked Rayleigh fractionation to show that changes in the fraction of water vapour rained out between tropical sources and the cave site could account for the observed variability in the cave records. Most modelling studies (Liu *et al.*²³ and references therein) support this idea, although most refer to the process as 'upstream depletion'. Cheng *et al.*⁴ proposed that changes in the fraction of low $\delta^{18}\text{O}$ monsoon rainfall in annual totals could also explain the record. Recent theoretical²⁴ and empirical²⁵ studies support this idea, with the latter showing that both

¹Institute of Global Environmental Change, Xi'an Jiaotong University, Xi'an 710049, China. ²Department of Earth Sciences, University of Minnesota, Minneapolis, Minnesota 55455, USA.

³Department of Earth Sciences, California State University, Dominguez Hills, Carson, California 90747, USA. ⁴Institut für Geologie, Universität Innsbruck, A-6020 Innsbruck, Austria. ⁵State Key Laboratory of Marine Geology, Tongji University, Shanghai 200092, China. ⁶College of Geography Science, Nanjing Normal University, Nanjing 210023, China. ⁷Earth Observatory of Singapore, Nanyang Technological University, 639798 Singapore.

processes can affect Chinese cave $\delta^{18}\text{O}$. For both, lower $\delta^{18}\text{O}$ implies higher spatially integrated monsoon rainfall between the tropical monsoon sources and the cave site and/or higher summer monsoon rainfall in the cave region. Thus, in this study, we use the terms ‘strong monsoon’ and ‘weak monsoon’ to refer to low and high cave $\delta^{18}\text{O}$, respectively, consistent with results from theoretical and empirical studies.

Our new records span from 640 to 330 kyr BP (before present, where present = AD 1950), which together with previous records (from 384 kyr BP to present), allow the construction of a composite AM $\delta^{18}\text{O}$ record, covering the past 640 kyr (Extended Data Fig. 4). The record is characterized by millennial-scale variations superimposed on a quasi-sine-wave-like orbital-scale variability that broadly tracks 21 July NHSI^{3,6} (Fig. 1). Removal of orbital-scale variations yields a record of the suborbital variability of the AM (the $\Delta\delta^{18}\text{O}$ record)⁸ (Extended Data Figs 5, 6). Detrending methods (for example, choice of insolation curve) could introduce artefacts in the $\Delta\delta^{18}\text{O}$ record, for which we tested by removing the orbital component of the record using insolation curves from a range of times encompassing the boreal summer months. Similar $\Delta\delta^{18}\text{O}$ power spectra independent of detrending curve suggest that this artefact is not significant. Detrending methods and sensitivity tests are described in the legends of Extended Data Figs 5, 6 and in Methods.

Timing and character of terminations

The gradual build-up and rapid termination of ice ages with an \sim 100-kyr cycle are a well-known feature of the past \sim 650 kyr (ref. 9). Although both glacial cycles and changes in eccentricity share common spectral power, the latter generates negligible change in insolation, thus presenting an enduring climate puzzle—the so-called ‘100-kyr problem’⁹. A number

of hypotheses have been put forth to address this problem. One hypothesis explains the 100-kyr cycle as an average of 4 to 5 discrete precession cycles, with missed beats in between^{10,11}. Another invokes 2 to 3 obliquity cycles^{12,13}, again with missed beats. Yet another invokes a combination of both obliquity and precession^{14–16}. Others call for interactions involving internal oscillations in the Earth system^{26,27}.

Cheng *et al.*⁴ have shown that each of the last four terminations is characterized by one or two WMIs, which coincide with HSs observed in North Atlantic marine cores^{7,8}. Abrupt WMI endings are synchronous with abrupt increases in atmospheric CH_4 in Antarctic ice cores⁴. Using these cave–marine and cave–ice core correlations, Cheng *et al.*⁴ placed the events observed in marine and ice cores on a cave chronology and made the following observations: the WMIs correlated with a good portion of each marine termination; the WMIs and the marine terminations took place at a time of rising NHSI; and most of the CO_2 rise associated with each termination took place during the WMIs (Extended Data Fig. 7). On the basis of these observations, Cheng *et al.*⁴ suggested that for each termination, the rise in insolation triggered the initial melting of the ice sheets. The North Atlantic cold anomaly that resulted from input of ice and meltwater rearranged oceanic and atmospheric circulation, causing the WMIs and resulting in the rise in atmospheric CO_2 . The latter, along with a continuing rise in insolation drove the termination^{4,28}.

The unparalleled length and temporal precision of our cave record allow us to extend the aforementioned approach to robustly test ideas about the classic ‘100-kyr problem’. Our data indicate that glacial terminations T-VII to T-V were also associated with WMIs (Fig. 2). The T-V WMI occurred between \sim 430.5 \pm 1.5 and \sim 426 \pm 2 kyr BP. The T-VI WMI, centred at 532.3 ± 3.5 kyr BP, has a duration of \sim 4.5 kyr,

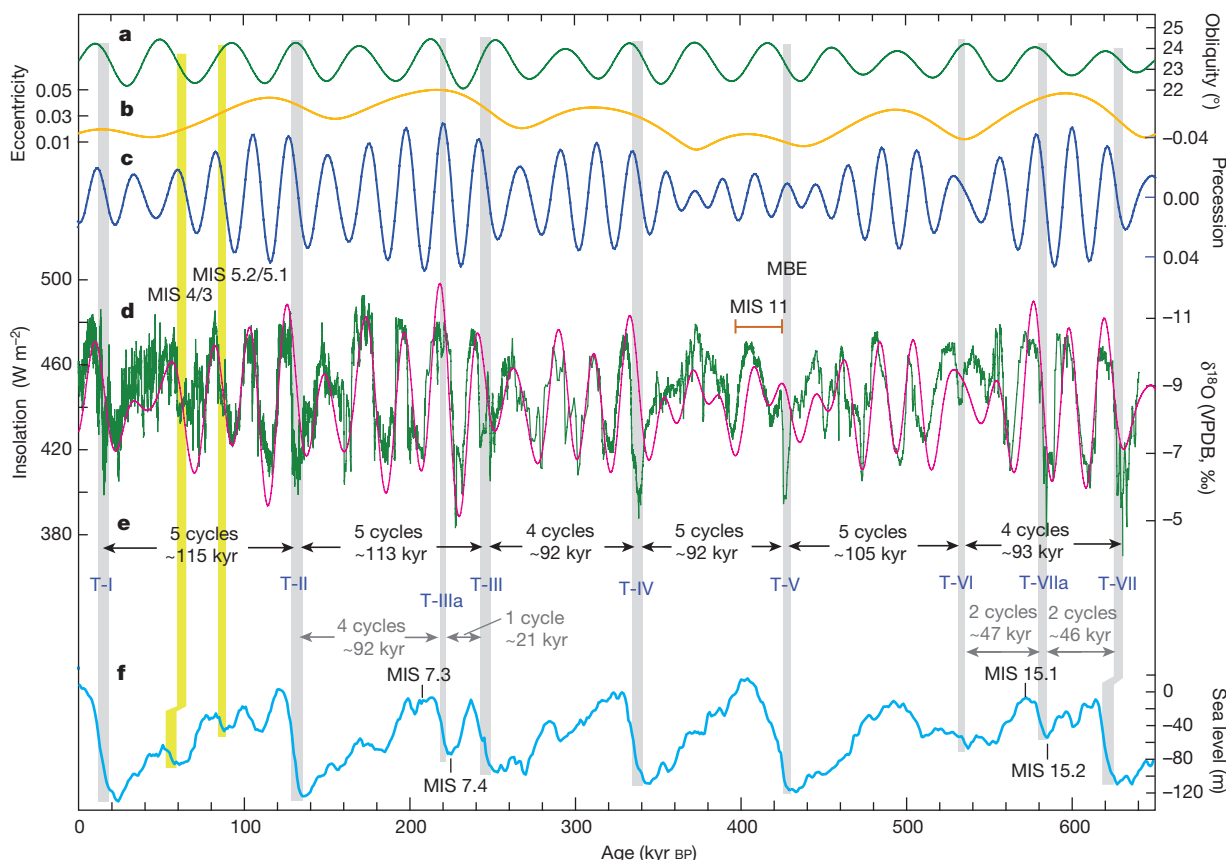


Figure 1 | Asian monsoon variations in the context of the Earth’s orbital parameters. **a–c**, Changes in obliquity (a), eccentricity (b) and precession⁴⁵ (c). **d**, The composite AM $\delta^{18}\text{O}$ record (green; this study) and 21 July insolation at 65° N (ref. 45; pink). **e**, Termination pacing and duration. Vertical bars mark the timing of WMIs correlated to glacial terminations

(grey) and two similar events (MIS 4/3 and 5.2/5.1 transitions) (yellow). The timing of T-IIIa-WMI in this study differs from the one described in ref. 4, although we consider the latter a plausible alternative (see main text and Extended Data Fig. 9). **f**, The composite sea level¹⁷. The timings of MBE, MIS 11, 7.3, 7.4, 15.1 and 15.2 are also depicted.

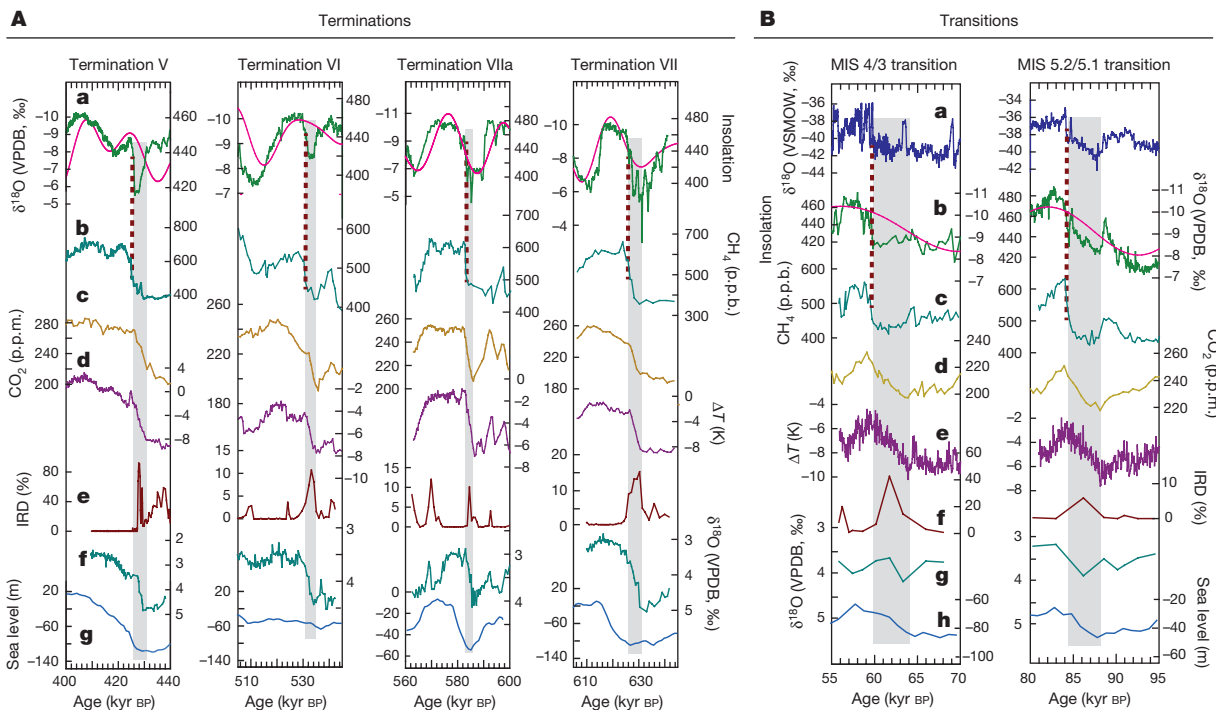


Figure 2 | Comparison of climate events surrounding terminations and other two millennial-scale events. **A.** Termination events surrounding T-V to T-VII. **a**, 21 July insolation at 65° N (pink, W m^{-2})⁴⁵ and the AM $\delta^{18}\text{O}$ record (green). **b**, **d**, EDC CH_4 (ref. 19) and relative temperature 18 records, respectively. **c**, The composite CO_2 record²⁰. The ice core ages (EDC3 chronology⁴⁶) around T-VI and T-VIIa are shifted to the older side by 3 and 2 kyr, respectively, to match the abrupt AM and CH_4 changes. **e**, **f**, Marine ODP980⁴⁷ (T-V) and U1314⁴⁸ (T-VI to T-VII) IRD and benthic $\delta^{18}\text{O}$ records, respectively. The marine records around T-V, T-VI, T-VIIa and T-VII were shifted to the older side by 6 kyr, the younger side by 2 kyr, older side by 2 kyr and older side by 3 kyr, respectively, to match corresponding IRD events to WMIs. **g**, The composite sea level¹⁷. **B.** Climate events surrounding MIS 4/3 and 5.2/5.1 transitions.

assuming a linear growth rate of sample SB-32 around this time period. The T-VII WMI is broadly similar to that of T-II, T-IV and T-V, ending abruptly at 627 ± 6 kyr BP. Each coincides presumably with a major HS, a sea level rise marking each glacial termination, a CO_2 rise, and an Antarctic temperature rise (Fig. 2). These observations, now for the past seven terminations, support the hypothesis that rising NHSI triggers an initial ice-sheet disintegration, which in turn perturbs the oceanic and atmospheric heat and carbon cycles, resulting in a CO_2 increase, which further drives the termination^{4,28}.

All seven terminations occurred during the rising limbs of NHSI separated by 4, 5, 5, 4, 5, and 5 precession cycles. The durations between successive terminations from T-VII to T-I were about 93, 105, 92, 92, 113 and 115 kyr, respectively, rather than strict 100-kyr cycles (Fig. 1). Thus, the ‘100-kyr cycle’ is an approximate average of intervals that are generally a little longer or shorter than 100 kyr. In addition, we characterize two ‘extra terminations’ revealed in marine records as follows: T-IIIa (ref. 12) occurred one precession cycle after T-III (between MIS 7.4 and 7.3), and T-VIIa occurred two precession cycles after T-VII (between MIS 15.2 and 15.1) (Fig. 1). Both exhibit a pattern of events similar to the seven main terminations, and large and comparable marine $\delta^{18}\text{O}$ or sea level changes¹⁷ (Figs 1, 2).

Each of the nine terminations is separated from adjacent terminations by an integral number of precession cycles. Thus, insolation intensity is critical in controlling the timing of terminations. In contrast, termination timing does not exhibit an obvious relationship to any particular portion of the obliquity or eccentricity cycles. For example, terminations take place when eccentricity is high (>0.02 : T-II, T-IIIa, T-III, T-IV, T-VIIa, T-VII) and when it is low (<0.02 : T-I, T-V,

a, Greenland ice core (NGRIP) $\delta^{18}\text{O}$ record⁴⁹. **b**, 21 July insolation at 65° N (pink, W m^{-2})⁴⁵ and AM $\delta^{18}\text{O}$ record (green). **c**, **e**, EDC CH_4 (ref. 19) and relative temperature 18 records, respectively. **d**, The composite CO_2 record²⁰. The ice core ages around MIS 4/3 and 5.2/5.1 transitions are shifted to the older side by 0.5 and 1 kyr respectively to match the abrupt AM and CH_4 changes. **f**, **g**, ODP980 IRD and benthic $\delta^{18}\text{O}$ records⁷, respectively. On the basis of correlations between IRD events and WMIs, the ODP980 ages are shifted to the younger side by ~ 4 and 3 kyr around MIS 4/3 and 5.2/5.1 transitions, respectively. **h**, The composite sea level¹⁷. Its chronology around the MIS 4/3 transition is shifted to the older side by ~ 5 kyr. Vertical grey bars indicate WMIs and corresponding events (CO_2 , Antarctic temperature, and North Atlantic IRD events). Dashed lines depict correlations between abrupt intensification in AM and CH_4 jump.

T-VI) (Fig. 1). Thus, changes in eccentricity are not, in a direct fashion, responsible for the pacing of the ‘100-kyr cycle’. Similarly, terminations take place as obliquity is increasing (T-IIIa, T-V, T-VII), decreasing (T-III, T-VI), and at peak or near peak values (T-I, T-II, T-IV, T-VIIa). Thus, as with eccentricity, obliquity does not pace terminations in a precise fashion. However, as none of the nine events takes place when obliquity is substantially below average, obliquity may play some causal role^{12–16}.

Pacemaker of millennial-scale events

A number of studies have focused on the cause of skipped precession and/or obliquity beats^{10,12,15} between terminations. More recent studies have referred to the events at some of these ‘missed beats’ as ‘low-amplitude versions of terminations’²⁹, ‘failed terminations’⁸, or ‘unfinished terminations’³⁰. For example, the MIS 4/3 and MIS 5.2/5.1 transitions took place at times of NHSI rise and have many of the features of full terminations, including periods of unusually weak monsoon (Fig. 2)—although, akin to T-VI, they do not result in extended interglacial conditions, but are characterized by significant sea level rise with larger marine $\delta^{18}\text{O}$ shifts than T-VI¹⁷ (Figs 1, 2). Explanations for full versus small-scale terminations focus on interplays and feedbacks among factors internal to the climate system, such as ice volume dynamics, in addition to orbital forcing^{15,31–34}.

As all full terminations and, at least, some small-scale terminations are associated with millennial-scale intervals of unusually weak monsoon, we examine the suborbital component of the full record to probe its relationship to orbital geometry. We start by removing orbital-scale frequencies to create a residual $\Delta\delta^{18}\text{O}$ record (Fig. 3), in which

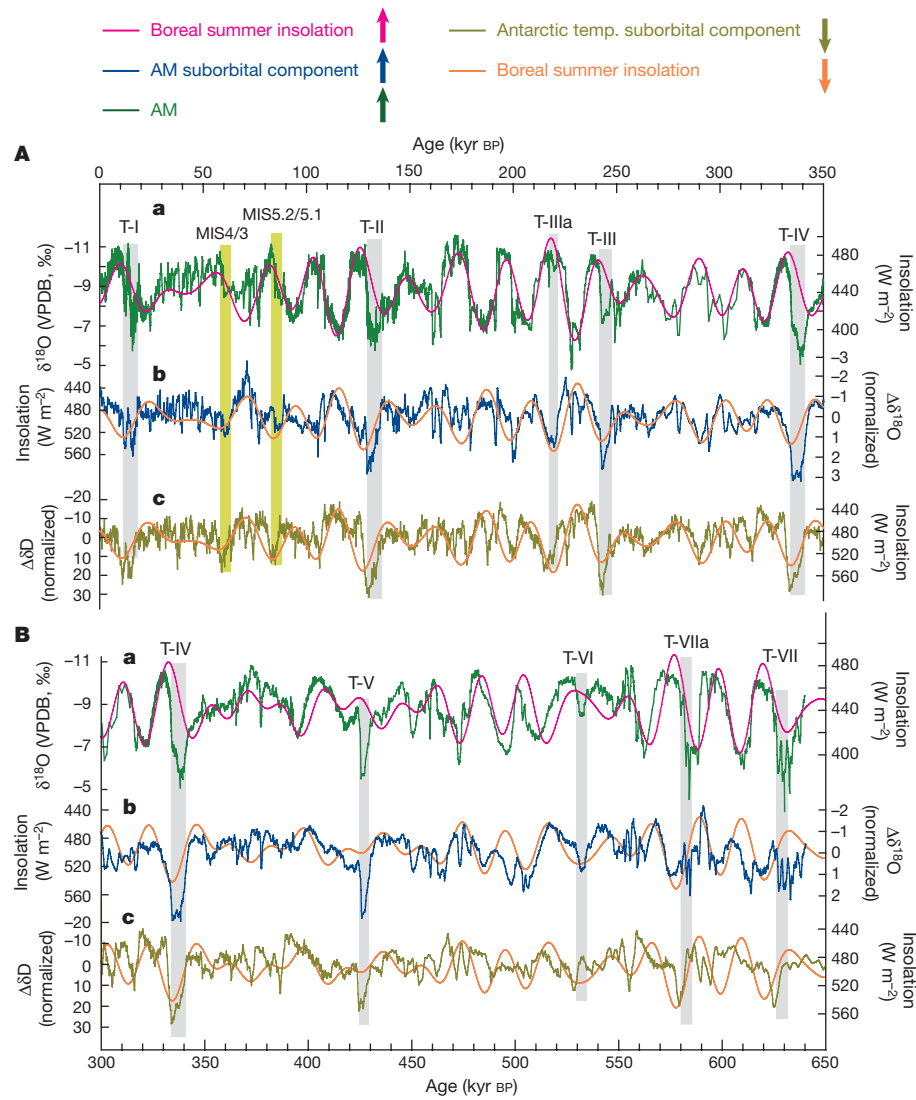


Figure 3 | Comparison of suborbital AM and Antarctic temperature variations. A, Interval from 350 to 0 kyr BP. B, Interval from 650 to 300 kyr BP. In both A and B: a, the composite AM $\delta^{18}\text{O}$ record (green) and 21 July insolation at 65°N (pink)⁴⁵; b, suborbital AM variation ($\Delta\delta^{18}\text{O}$, detrended from the composite $\delta^{18}\text{O}$ record by subtracting 21 July insolation at 65°N ; see Methods); c, Antarctic suborbital temperature

suborbital variability is clearly observed⁸. Prominent features are the aforementioned WMIs, millennial-scale features characterized by large positive anomalies in $\delta^{18}\text{O}$ at terminations. A closer look shows many smaller amplitude, millennial-scale, high- $\delta^{18}\text{O}$ events throughout, including those correlated with small-scale terminations. We infer that these events may share a similar origin with the WMIs, since the pattern of events surrounding these smaller events is indeed similar to terminations, including some for which the marine $\delta^{18}\text{O}$ /sea level shift is comparable or larger than that of T-VI (Fig. 2). Specifically, we infer that the smaller amplitude events are caused by the decay of the northern ice sheets, resulting in the flux of ice and meltwater into the North Atlantic; the ensuing slowdown in Atlantic Meridional Overturning Circulation (AMOC) generates a cold anomaly over the North Atlantic. Through an atmospheric teleconnection, the cold anomaly results in a weaker AM, recorded as a high $\delta^{18}\text{O}$ anomaly in our record (Fig. 2)^{1,4,28}.

Spectral analysis of the $\Delta\delta^{18}\text{O}$ record reveals strong power in the precession band, with the suborbital component of the AM close to anti-phased with (that is, $\sim 180^\circ$ from) 21 June insolation (Fig. 4b). The suborbital spectrum also exhibits weaker but significant power in the obliquity band, again with the suborbital component close to

variation ($\Delta\delta\text{D}$ record detrended from the δD record¹⁸; see Methods). Orange curves show 21 June insolation at 65°N (ref. 45) on a reversed scale (increasing down) for comparison. A remarkable similarity is evident between suborbital variations in AM $\Delta\delta^{18}\text{O}$ and Antarctic $\Delta\delta\text{D}$ records (also see Extended Data Fig. 8).

anti-phased with obliquity. Thus, insolation modulates the suborbital component of AM variability, but in the opposite sense from the more direct control of orbital-scale variability of the AM. We take these observations to indicate that high NHSI, whether in the precession or obliquity bands, favours the disintegration of the northern ice sheets and the release of ice and meltwater into the North Atlantic. This signal then propagates through the ocean and atmosphere as outlined above (and previously described for WMIs), resulting in the weakening of the monsoon^{4,28}. Inspection of Fig. 3 shows that the relationship is pervasive throughout the record.

We have performed a similar analysis on the Antarctic δD (a temperature proxy) record¹⁸, by first removing low frequency, orbital-scale variability, then examining the power spectrum of the resulting suborbital variability³⁵ (Fig. 4 and Extended Data Fig. 8). The suborbital-scale Antarctic temperature and AM records are remarkably similar, with the suborbital components of the AM and Antarctic temperature anti-correlated. We attribute this relationship to the bi-polar seesaw mechanism³⁶. As input of meltwater and ice into the North Atlantic is the presumed source of both sets of suborbital variability, it is not surprising that the suborbital component of Antarctic temperature

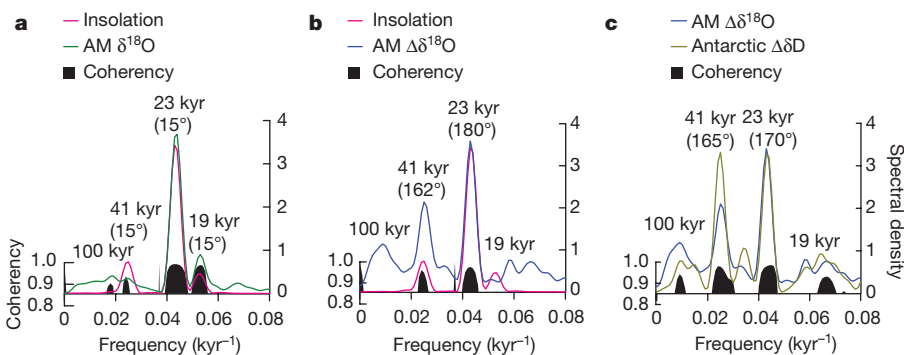


Figure 4 | Cross-spectral comparison. Compared are insolation, AM, detrended (suborbital) AM and detrended (suborbital) Antarctic $\Delta\delta^{18}\text{O}$ records over the past 640 kyr BP. **a**, Spectral analysis results of 21 July insolation at 65° N (ref. 45; pink) and AM $\delta^{18}\text{O}$ (green), and their coherence spectra (black). **b**, Spectral analysis results of 21 June insolation at 65° N (ref. 45; pink) and detrended AM $\Delta\delta^{18}\text{O}$ (blue), and their coherence spectra (black). **c**, Spectral analysis results of detrended AM $\Delta\delta^{18}\text{O}$ (blue) and detrended Antarctic $\Delta\delta\text{D}$ records (olive), and their coherence spectra (black). Coherence spectra are at 80% confidence level. Numbers in parentheses show phase differences in degrees between two spectra at precession (~23 and 19 kyr) and obliquity (~41 kyr) bands. Precession periodicity of ~23 kyr is significant in all four datasets. The variations in both AM $\Delta\delta^{18}\text{O}$ and Antarctic $\Delta\delta\text{D}$ records also show significant power at obliquity band. Cross-spectrum analyses reveal a phase coherency at precession band between AM $\delta^{18}\text{O}$ record and 21 July insolation and between Antarctic $\Delta\delta\text{D}$ and 21 June insolation. AM $\Delta\delta^{18}\text{O}$ is nearly anti-phased with Antarctic $\Delta\delta\text{D}$ and 21 June insolation at precession band.

variability also exhibits significant power in the precession and obliquity bands nearly in phase with NHSI. These results suggest that the change of NHSI induced by precession (with lesser involvement of obliquity) is the major external pacemaker of both conventional and the ‘small-scale’ termination events, which coincide with the large-scale weakening of the AM and warming in Antarctica^{4,8,28,30}.

While the sequence of events surrounding each positive AM $\delta^{18}\text{O}$ anomaly is similar, the relative amplitudes of these events vary (Fig. 3). Hence, the key issue is not why terminations are spaced by some discrete number of precession cycles, but rather why some of the events developed ultimately into full terminations. The possibility of a certain event evolving into a full termination may depend on the state of the climate system at that time—for example, favourable internal interplays/feedbacks of ice-sheet dynamics and size, insolation, and ocean

and CO₂ feedbacks^{4,28,30–34}. For example, as pointed out by Raymo³¹, a large and isostatically-compensated ice sheet would be relatively vulnerable to decay. In this scenario, precession cycles would be skipped or a ‘termination’ would be unfinished until the ice sheets were in such a state, on average after about 100 kyr. Regardless of exact mechanisms, the WMIs and smaller analogues to WMIs are indeed paced primarily by precession cycles, suggesting that the 100 kyr in the ‘100-kyr problem’ represents an approximate mean of integral numbers of precession cycles between terminations.

Mid-Brunhes event and MIS 11

Our record covers much of the time since the so-called Mid-Pleistocene revolution¹¹ and crosses the MBE³⁷. The MBE is contemporaneous with T-V, a portion of which correlates with a WMI in our record. The

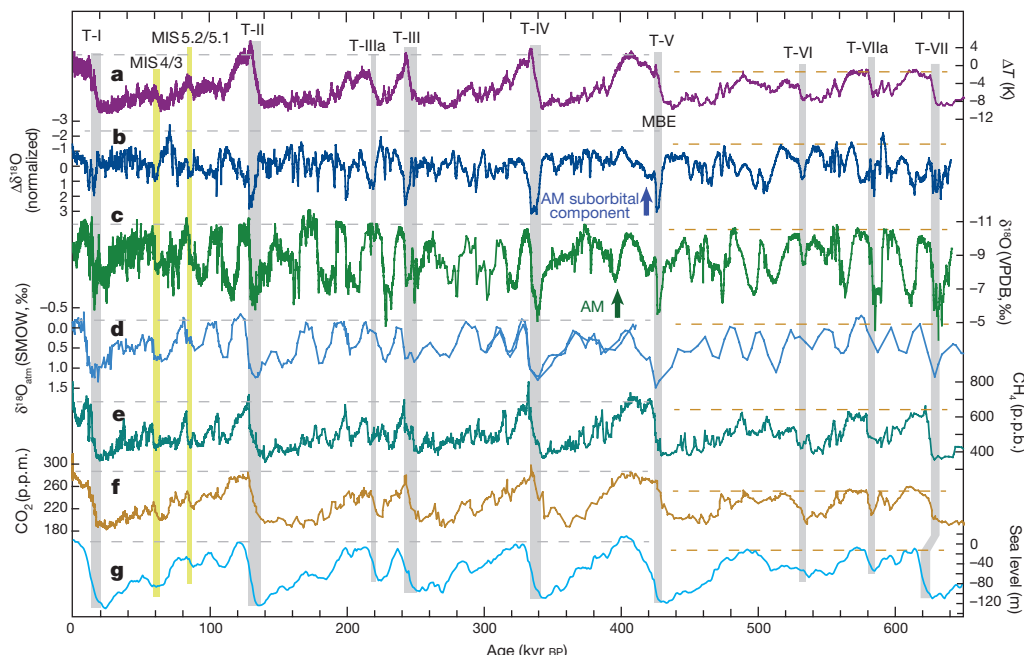


Figure 5 | Comparison of climate records across the MBE. **a, d, e, f**, Relative temperature¹⁸, $\delta^{18}\text{O}_{\text{atm}}$ (ref. 50) and CH₄ (ref. 19) records, respectively, from Antarctic EDC ice core records (EDC3 chronology⁴⁶). **b**, The suborbital variations in the AM $\Delta\delta^{18}\text{O}$ record. **c**, The orbital variations in the AM $\delta^{18}\text{O}$ record. **f**, The composite CO₂ record²⁰.

g, The composite sea level¹⁷. Horizontal dashed lines indicate interglacial amplitude shift across the MBE. Vertical bars indicate WMIs and associated T-I to T-VII (grey) as well as MIS 4/3 and 5.2/5.1 transitions (yellow).

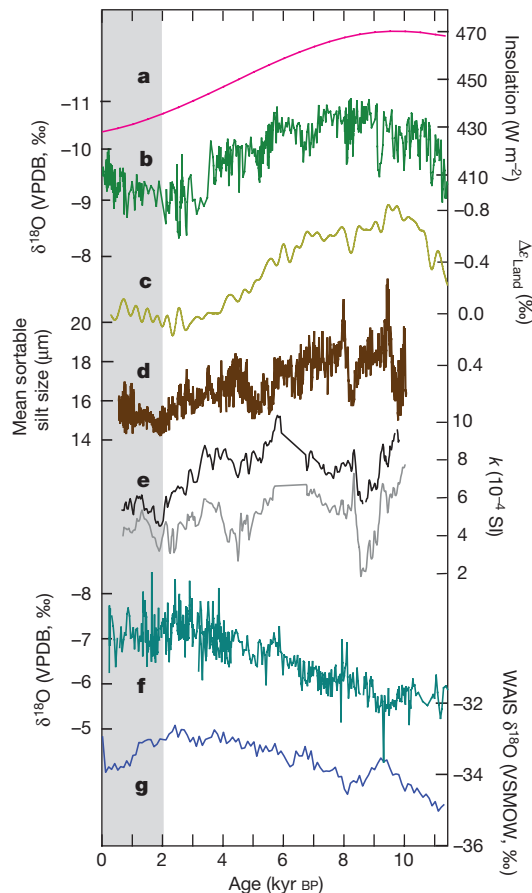


Figure 6 | Comparison among Holocene records. **a**, 21 July insolation at 65° N (ref. 45). **b**, The composite AM $\delta^{18}\text{O}$ records. **c**, The Holocene terrestrial $\delta^{18}\text{O}/\delta^{16}\text{O}$ fractionation variation³⁹. **d**, The mean grain size of sortable silt (10–63 μm) for North Atlantic sediment cores MD2251 and MD2024, a proxy of North Atlantic Deep Water formation⁴³. **e**, North Atlantic deep-flow dynamic proxy (low field magnetic susceptibility, k) records from cores CH77-02 (black) and MD08-3182Cq (grey)⁴⁴. **f**, The South American monsoon record⁴⁰. **g**, The $\delta^{18}\text{O}$ record (WAIS, a temperature proxy) from western Antarctica⁴¹. Vertical bar depicts the ‘2-kyr shift’.

amplitude of glacial–interglacial cycles in CO_2 , Antarctic temperature, and global ice volume (or sea level) increased substantially after the MBE. In contrast, interglacial CH_4 , $\delta^{18}\text{O}_{\text{atm}}$, and AM intensity in our records are only slightly enhanced across the MBE (Fig. 5), similar to another hydrological record reported previously from low latitude³⁸. Thus, changes in the AM behaviour across the MBE were not as large as changes at high latitudes and in CO_2 . In addition, there are numerous examples of high AM intensity during glacial periods when ice volume was large and CO_2 was low (Fig. 5). Furthermore, the initial increase of the AM tends to start at each insolation minimum and in some cases does not appear to correlate with any obvious ice-volume and/or CO_2 changes (Extended Data Fig. 9). These observations indicate that, at the orbital scale, the AM and associated climate and atmospheric chemistry change are largely controlled by NHSI⁶. However, the post-MBE WMIs associated with glacial terminations are much more intense (Fig. 5b). It is possible that this change results from a shift in the response time of the AM to NHSI. However, in our view, a more likely cause is the observed shift to higher maximum ice volume resulting in higher ice and meltwater flux during terminations and larger perturbations of the climate system, including more extreme WMIs. In this light, T-V has the first of the large post-MBE-style WMIs.

Our new data also include a well-dated record of AM variability during MIS 11. Orbital parameters for MIS 11 are closer to those of

the Holocene than for other recent interglacial periods, making it an analogue for the Holocene and future climate²¹. However, uncertainties remain regarding its timing and duration. We estimate the beginning of AM MIS 11 to be the abrupt end of the T-V WMI at 426 ± 1 kyr BP. If we take the end to be the AM minimum at 396 ± 3 kyr BP (about the time of the half-height of the benthic $\delta^{18}\text{O}$ MIS 11/10 shift¹⁷), the duration is 30 ± 4 kyr. If we take the end to be the time of the half-height of the AM shift after the MIS 11 AM peak (at 399 ± 3 kyr BP), the duration is 27 ± 4 kyr. These estimates are consistent within age uncertainties with the duration of MIS 11 defined by other less precisely dated records²¹.

The ‘2-kyr shift’

Over the past ~ 2 kyr the AM has increased in an anomalous fashion relative to the downward trend in NHSI (Fig. 6 and Extended Data Fig. 10). This trend relates to climate change elsewhere around the world in much the same way as the millennial-scale shifts over the past 640 kyr. We refer to this late Holocene anomaly as the ‘2-kyr shift’. The ‘2-kyr shift’ is more than just a regional shift in the AM as evidenced by an in phase, positively-correlated shift in the $\delta^{18}\text{O}$ of atmospheric O_2 (ref. 39), which integrates a broad swath of the globe and may, in large part, respond to AM intensity. The AM shift also anti-correlates with records of the South American monsoon⁴⁰ and temperature over some parts of Antarctica⁴¹ (Fig. 6) — a pattern similar to the one observed for millennial-scale events throughout much of the past several hundred kyr. A change in AMOC has been suggested as a key process that may explain aspects of such millennial-scale changes⁴². In this regard, two studies^{43,44} show generally decreasing AMOC for several millennia before ~ 2 kyr BP, then constant or perhaps slightly increasing AMOC for the last 2 kyr (Fig. 6). Thus, it is plausible that the origin of the ‘2-kyr shift’ is a progressive increase in the rate of AMOC over the past 2 kyr. Nevertheless, observational and modelling studies are critically needed to further assess the ‘2-kyr shift’.

Online Content Methods, along with any additional Extended Data display items and Source Data, are available in the online version of the paper; references unique to these sections appear only in the online paper.

Received 26 January; accepted 18 May 2016.

- Cheng, H., Sinha, A., Wang, X. F. & Cruz, F. W. The global paleomonsoon as seen through speleothem records from Asia and South America. *Clim. Dyn.* **39**, 1045–1062 (2012).
- Wang, Y. J. et al. A high-resolution absolute-dated Late Pleistocene monsoon record from Hulu Cave, China. *Science* **294**, 2345–2348 (2001).
- Wang, Y. J. et al. Millennial- and orbital-scale changes in the East Asian Monsoon over the past 224,000 years. *Nature* **451**, 1090–1093 (2008).
- Cheng, H. et al. Ice age terminations. *Science* **326**, 248–252 (2009).
- Cheng, H. et al. Improvements in ^{230}Th dating, ^{230}Th and ^{234}U half-life values, and U-Th isotopic measurements by multi-collector inductively coupled plasma mass spectrometry. *Earth Planet. Sci. Lett.* **371–372**, 82–91 (2013).
- Kutzbach, J. E., Liu, X. D., Liu, Z. Y. & Chen, G. S. Simulation of the evolutionary response of global summer monsoons to orbital forcing over the past 280,000 years. *Clim. Dyn.* **30**, 567–579 (2008).
- McManus, J. F., Oppo, D. W. & Cullen, J. L. A. 0.5-million-year record of millennial-scale climate variability in the North Atlantic. *Science* **283**, 971–975 (1999).
- Barker, S. et al. 800,000 years of abrupt climate variability. *Science* **334**, 347–351 (2011).
- Hays, J. D., Imbrie, J. & Shackleton, N. J. Variations in the Earth’s orbit: pacemaker of the ice ages. *Science* **194**, 1121–1132 (1976).
- Raymo, M. E. Glacial puzzles. *Science* **281**, 1467–1468 (1998).
- Maslin, M. A. & Ridgewell, A. in *Early–Middle Pleistocene Transitions: The Land–Ocean Evidence* (eds Head, M. J. & Gibbard, P. L.) 19–34 (Vol. 247, Spec. Publ. Geol. Soc. Lond., 2005).
- Huybers, P. & Wunsch, C. Obliquity pacing of the late Pleistocene glacial terminations. *Nature* **434**, 491–494 (2005).
- Bintanja, R. & van de Wal, R. S. W. North American ice-sheet dynamics and the onset of 100,000-year glacial cycles. *Nature* **454**, 869–872 (2008).
- Imbrie, J. & Imbrie, J. Modeling the climatic response to orbital variations. *Science* **207**, 943–953 (1980).
- Paillard, D. The timing of Pleistocene glaciations from a simple multiple-state climate model. *Nature* **391**, 378–381 (1998).
- Huybers, P. Combined obliquity and precession pacing of late Pleistocene deglaciations. *Nature* **480**, 229–232 (2011).

17. Spratt, R. M. & Lisicki, L. E. A Late Pleistocene sea level stack. *Clim. Past Discuss.* **11**, 3699–3728 (2015).
18. Jouzel, J. et al. Orbital and millennial Antarctic climate variability over the past 800,000 years. *Science* **317**, 793–796 (2007).
19. Loulergue, L. et al. Orbital and millennial-scale features of atmospheric CH₄ over the past 800 000 years. *Nature* **453**, 383–386 (2008).
20. Bereiter, B. et al. Revision of the EPICA Dome C CO₂ record from 800 to 600 kyr before present. *Geophys. Res. Lett.* **42**, 542–549 (2015).
21. Candy, I., Schreve, D. C., Sherriff, J. & Tye, G. J. Marine Isotope Stage 11: Palaeoclimates, palaeoenvironments and its role as an analogue for the current interglacial. *Earth Sci. Rev.* **128**, 18–51 (2014).
22. Yuan, D. X. et al. Timing, duration, and transitions of the Last Interglacial Asian monsoon. *Science* **304**, 575–578 (2004).
23. Liu, Z. Y. et al. Chinese cave records and the East Asia Summer Monsoon. *Quat. Sci. Rev.* **83**, 115–128 (2014).
24. Chiang, J. C. H. et al. Role of seasonal transitions and westerly jets in East Asian paleoclimate. *Quat. Sci. Rev.* **108**, 111–129 (2015).
25. Orland, I. J. et al. Direct measurements of deglacial monsoon strength in a Chinese stalagmite. *Geology* **43**, 555–558 (2015).
26. Saltzman, B., Hansen, A. & Maasch, K. The late Quaternary glaciations as the response of a three-component feedback system to Earth-orbital forcing. *J. Atmos. Sci.* **41**, 3380–3389 (1984).
27. Toggweiler, J. R. Origin of the 100,000-year timescale in Antarctic temperatures and atmospheric CO₂. *Paleoceanography* **23**, PA2211 (2008).
28. Denton, G. H. et al. The last glacial termination. *Science* **328**, 1652–1656 (2010).
29. Wolff, E. W., Fischer, H. & Röhlisberger, R. Glacial terminations as southern warmings without northern control. *Nat. Geosci.* **2**, 206–209 (2009).
30. Schaefer, J. M. et al. The southern glacial maximum 65,000 years ago and its unfinished termination. *Quat. Sci. Rev.* **114**, 52–60 (2015).
31. Raymo, M. E. The timing of major climate terminations. *Paleoceanography* **12**, 577–585 (1997).
32. Imbrie, J. et al. On the structure and origin of major glaciation cycles 2. The 100,000-year cycle. *Paleoceanography* **8**, 699–735 (1993).
33. Parrenin, F. & Paillard, D. Amplitude and phase of glacial cycles from a conceptual model. *Earth Planet. Sci. Lett.* **214**, 243–250 (2003).
34. Abe-Ouchi, A. et al. Insolation-driven 100,000-year glacial cycles and hysteresis of ice-sheet volume. *Nature* **500**, 190–193 (2013).
35. Siddall, M., Rohling, E. J., Blunier, T. & Spahni, R. Patterns of millennial variability over the last 500 ka. *Clim. Past* **6**, 295–303 (2010).
36. Broecker, W. S. Paleocean circulation during the last deglaciation: a bipolar seesaw? *Paleoceanography* **13**, 119–121 (1998).
37. Jansen, J. H. F., Kuijpers, A. & Troelstra, S. R. A Mid-Brunhes climatic event: long-term changes in global atmosphere and ocean circulation. *Science* **232**, 619–622 (1986).
38. Meckler, A. N., Clarkson, M. O., Cobb, K. M., Sodemann, H. & Adkins, J. F. Interglacial hydroclimate in the tropical West Pacific through the late Pleistocene. *Science* **336**, 1301–1304 (2012).
39. Severinghaus, J. P., Beaudette, R., Headley, M. A., Taylor, K. & Brook, E. J. Oxygen-18 of O₂ records the impact of abrupt climate change on the terrestrial biosphere. *Science* **324**, 1431–1434 (2009).
40. van Breukelen, M. R., Vonhof, H. B., Hellstrom, J. C., Wester, W. C. G. & Kroon, D. Fossil dripwater in stalagmites reveals Holocene temperature and rainfall variation in Amazonia. *Earth Planet. Sci. Lett.* **275**, 54–60 (2008).
41. WAIS Divide Project Members. Onset of deglacial warming in West Antarctica driven by local orbital forcing. *Nature* **500**, 440–444 (2013).
42. Broecker, W. S. & Denton, G. H. The role of ocean-atmosphere reorganizations in glacial cycles. *Geochim. Cosmochim. Acta* **53**, 2465–2501 (1989).
43. Hoogakker, B. A. A. et al. Dynamics of North Atlantic Deep Water masses during the Holocene. *Paleoceanography* **26**, PA4214 (2011).
44. Kissel, C., Toer, A. V., Laj, C., Cortijo, E. & Michel, E. Variations in the strength of the North Atlantic bottom water during Holocene. *Earth Planet. Sci. Lett.* **369–370**, 248–259 (2013).
45. Berger, A. Long-term variations of caloric insolation resulting from the Earth's orbital elements. *Quat. Res.* **9**, 139–167 (1978).
46. Parrenin, F. et al. The EDC3 chronology for the EPICA Dome C ice core. *Clim. Past* **3**, 485–497 (2007).
47. Alonso-Garcia, M. et al. Ocean circulation, ice sheet growth and interhemispheric coupling of millennial climate variability during the Mid-Pleistocene (ca. 800–400 ka). *Quat. Sci. Rev.* **30**, 3234–3247 (2011).
48. Wright, A. K. & Flower, B. P. Surface and deep ocean circulation in the subpolar North Atlantic during the mid-Pleistocene revolution. *Paleoceanography* **17**, 1068 (2002).
49. Wolff, E. W., Chappellaz, J., Blunier, T., Rasmussen, S. O. & Svensson, A. Millennial-scale variability during the last glacial: The ice core record. *Quat. Sci. Rev.* **29**, 2828–2838 (2010).
50. Landais, A. et al. What drives the millennial and orbital variations of δ¹⁸O_{atm}? *Quat. Sci. Rev.* **29**, 235–246 (2010).

Supplementary Information is available in the online version of the paper.

Acknowledgements This work was supported by China grants NBRP 2013CB955902, NSFC 41230524, 4157020432 and 41561144003, US NSF grants 0502535, 1103404, 0823554, 1003690, 1137693 and 1317693 and Singapore grant NRF-NRFF2011-08. We thank M. Siddall for help with analysis of the millennial-scale variability of the Antarctic temperature record and A. P. Roberts for converting the ice core chronology.

Author Contributions H.C. designed the research and experiments; H.C., R.L.E. and A.S. wrote the manuscript, which was edited by all of the co-authors; L.Y., S.C. and A.S. did the spectral analysis; X.K., Y.W. and S.C. provided the cave samples; H.C. did the ²³⁰Th dating work; and C.S., X.K., M.K., Y.N. and H.Z. contributed to oxygen isotope measurements. All authors discussed the results and provided input to the manuscript and technical aspects of the laboratory analyses.

Author Information Reprints and permissions information is available at www.nature.com/reprints. The authors declare no competing financial interests. Readers are welcome to comment on the online version of the paper. Correspondence and requests for materials should be addressed to H.C. (cheng021@mail.xjtu.edu.cn) or R.L.E. (edwar001@umn.edu).

Reviewer Information *Nature* thanks C. Buzert, A. N. Meckler and the other anonymous reviewer(s) for their contribution to the peer review of this work.

METHODS

²³⁰Th dating. Four stalagmite samples, SB-12, SB-14, SB-32 and SB-58, were collected from Sanbao Cave, Hubei, China. The sampling location is ~1,500 m from the entrance, marked by a relative humidity of ~100%. The stalagmites were cut into halves along their growth axes and polished. A total of 196 sub-samples (25, 69, 84 and 18 for SB-12, SB-14, SB-32 and SB-58, respectively) were drilled for ²³⁰Th dating (Supplementary Table 1). In addition, 9 dates were also obtained for stalagmite D8 from Dongge Cave, China. The dating work was performed at the Minnesota Isotope Laboratory, University of Minnesota (Sanbao samples) and the Institute of Global Environmental Change, Xi'an Jiaotong University, Xi'an, China (Dongge samples). The ²³⁰Th dating techniques are essentially identical in the two laboratories. All measurements were made on Thermo-Finnigan Neptune multi-collector inductively coupled plasma mass spectrometers using the recently improved technique⁵. We use standard chemistry procedures to separate U and Th as described in ref. 51. The isotope dilution method with a triple-spike ²²⁹Th–²³³U–²³⁶U was employed to correct for instrumental fractionation and determine U and Th isotopic ratios and concentrations. The instrumentation, standardization and half-lives are reported in refs 5 and 52. All U and Th isotopes were measured either on the Faraday cups (larger sample size) or on a MasCom multiplier behind the retarding potential quadrupole in the peak-jumping mode (smaller sample size). We followed similar procedures of characterizing the multiplier as described in ref. 52. Uncertainties in U and Th isotopic data were calculated offline at the 2σ level, including corrections for chemistry/instrument blanks, multiplier dark noise, abundance sensitivity, tails, and contents of the same four nuclides in the spike solution^{5,52}. Corrected ²³⁰Th ages assume an initial ²³⁰Th/²³²Th atomic ratio of $(4.4 \pm 2.2) \times 10^{-6}$, the values for a material at secular equilibrium with the bulk Earth ²³²Th/²³⁸U value of 3.8. The correction is negligible because the samples used in this study have high U and low Th contents. The age model for each stalagmite is established by either linear interpolation or polynomial fitting (Extended Data Fig. 3).

Stable isotope analysis. Oxygen isotopic composition ($\delta^{18}\text{O}$) of stalagmite samples was analysed at three laboratories—Universität Innsbruck, Austria (the top 12.4 cm of sample SB-14, ~2,400 subsamples), Nanjing Normal University, China (133, 585, 140 and 155 subsamples from SB-12, SB-14, SB-32 and SB-58, respectively), and Xi'an Jiaotong University (80 subsamples from D8). Results are reported in per mil (‰), relative to the Vienna PeeDee Belemnite (VPDB) standard. We obtained a total of ~3,360 stable isotope data (Supplementary Table 1). The techniques used in Universität Innsbruck are described in ref. 53. Stable isotope samples were micromilled perpendicularly to the extension axes of the stalagmites at 0.05 to 0.1 mm increments and analysed using an on-line carbonate preparation system (Gasbench II) interfaced with an isotope ratio mass spectrometer (Delta^{plus}XL). The long-term reproducibility is ~0.08‰ (1σ). The stable isotope measurements in Nanjing Normal University were made on a Thermo-Finnigan MAT-253 mass spectrometer fitted with a Kiel Carbonate Device III. Stable isotope samples were milled using carbide dental burrs ranging in size from 0.3 to 0.5 mm along the central growth axis of stalagmites. Samples were calibrated against the NBS-19 standard. Standard measurements have an analytical precision of typically 0.08‰ (1σ). The measurements in Xi'an Jiaotong University were made on a Thermo-Finnigan MAT-253 mass spectrometer fitted with a Kiel Carbonate Device IV. Stable isotope samples were micromilled perpendicularly to the extension axes of the stalagmite D8 at 0.05 to 0.1 mm increments. Duplicate measurements of NBS19 and TT1 standards show a long-term reproducibility of ~0.1‰ or better (1σ).

Composite Chinese cave $\delta^{18}\text{O}$ record over the last 640 kyr. The composite AM $\delta^{18}\text{O}$ record over the last 640 kyr is based on previously published data (<384 kyr BP)^{2,4,22,54,55} and new data from four Sanbao stalagmite records (≥ 384 kyr BP) from this study (SB-12, SB-14, SB-32 and SB-58). The composite $\delta^{18}\text{O}$ record is constructed based on two criteria to select temporally-overlapped records—the dating control and the temporal resolution (see details in Supplementary Table 1). The new $\delta^{18}\text{O}$ record from Dongge Cave (D8) replaces the previously published records between 217.2 and 225.3 kyr BP, as the age control of stalagmite D8 is superior for this time period. The overall average temporal-resolution of the record is 85 years. The lowest resolution (~500 years) is in the interval of the previous record between ~305 and 260 kyr BP, and the rest of time periods have resolution better than 200 years (Supplementary Table 1).

Normalization and detrending. In order to remove the orbital insolation component from the composite AM $\delta^{18}\text{O}$ data, we used two different methods, z-standard and principal components analysis (PCA). For the z-standard method, we first converted the composite $\delta^{18}\text{O}$ data to z-standard by using the mean and standard deviation of each data set (that is, zero-mean normalization). An average data resolution of 200 years was used to allow point-to-point alignment. The detrended $\delta^{18}\text{O}$ data ($\Delta\delta^{18}\text{O}$) was obtained by subtracting 21 July insolation at 65°N (refs 3, 6)

from the $\delta^{18}\text{O}$ record after standardization and equal spacing to the 200-year interval. Insolation is normalized to be equal in magnitude to $\delta^{18}\text{O}$ and assigned an opposite algebraic sign: $\Delta\delta^{18}\text{O} = \delta^{18}\text{O} - (-\text{NHSI}_{\text{norm}}) = \delta^{18}\text{O} + \text{NHSI}_{\text{norm}}$. For the PCA method, we also converted the composite AM $\delta^{18}\text{O}$ data in 200-year time-steps to synthesize the insolation in the same time-steps. We then standardized the common principal components obtained from the insolation time series and the original AM records. The PCAs are computed by using SPSS 15.0. The difference between the AM record and the common principal components was then used to characterize the millennial-scale variability. In addition to 21 July insolation, we also calculated the detrended results by using different insolation curves (21 June, 6 July and 6 August insolation at 65°N), in order to test the sensitivity. We found that the results are similar (Extended Data Figs 5 and 6). The methods and results used here are essentially similar to those described in ref. 8. The $\Delta\delta^{18}\text{O}$ record obtained by the z-standard method is used in the figures for comparison.

The method used for detrending of the Antarctic δD record from EDC ice cores (Extended Data Fig. 8) was modified from that described in ref. 35. We first defined the long-term trend from the δD record by binning the combined data using the mean over 0.1-kyr intervals on 6-kyr windows on each data point. The window length of 6 kyr was chosen to effectively remove the glacial–interglacial trend³⁵. Sensitivity tests through varying the length of the 6-kyr window by a factor of two (that is, between 3 and 12 kyr) show no substantial impact on the spectral results. Second, we obtained the detrended record ($\Delta\delta\text{D}$) by subtracting the long-term trend from the δD record. Our results are similar to those described in ref. 35.

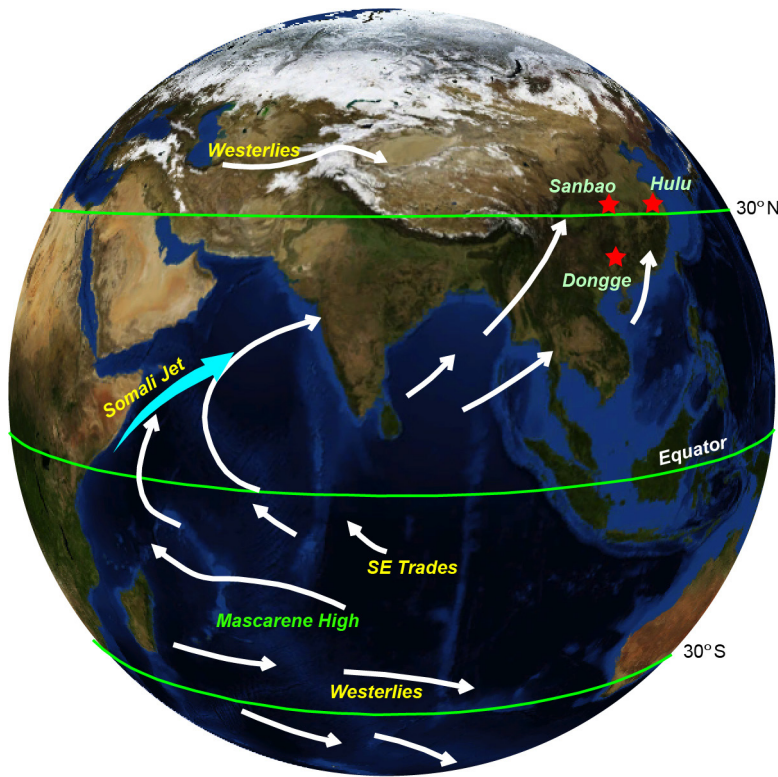
Spectrum analysis. In order to identify periodic components in the spectrum of our AM $\Delta\delta^{18}\text{O}$ record, we applied the spectral analysis following the Blackman–Tukey method⁵⁶ using the ARAND software package. The following parameters were used to optimize bias/variance properties of spectrum estimates: number of lags = 1,200 (~1/3 length of record) and samples per analysis = 2,000. The results show that the $\Delta\delta^{18}\text{O}$ records have significant power at ~23 kyr, weaker power at ~41 kyr and insignificant power at ~100 kyr (Fig. 4, Extended Data Figs 5 and 6).

Cross-spectrum analysis results are obtained between AM $\delta^{18}\text{O}$, AM $\Delta\delta^{18}\text{O}$, Antarctic $\Delta\delta\text{D}$, and insolation records over the last 640 kyr using the ARAND software package. Detailed methods are described in ref. 56. The coherency spectra are compared with the 80% non-zero coherency level, resulting in a dominant cyclicity of ~23 kyr for all the analysis results (Fig. 4, Extended Data Figs 5, 6 and 8). However, the deviation of the phase spectrum from the zero-phase line suggests that the detrended AM records may have different phases relative to insolation at precession bands (~23 kyr), depending on the time of insolation used in the detrending process. If 21 July insolation is used for the detrending, as suggested by both empirical³ and theoretical⁶ studies, the millennial variability in the detrended AM record ($\Delta\delta^{18}\text{O}$ record) is then nearly anti-phase with 21 June insolation ($\sim 180^\circ \pm 10^\circ$ or ± 1 kyr). In addition, because absolute ²³⁰Th dating errors increase progressively with sample age, we also tested all the spectrum analysis results by using the AM record only for the last 480 kyr BP when the dating errors are smaller. In all cases, we essentially obtained the same analysis results.

Chronologies. We use original chronologies of other climate records in most cases, including the Greenland ice core record (GICC05 chronology)⁴⁹, Antarctic ice core CO₂, CH₄ and $\delta^{18}\text{O}_{\text{atm}}$, dust and temperature records (EDC3 chronology)⁴⁶, the composite CO₂ record (AICC2012 chronology)²⁰, and the stacked benthic $\delta^{18}\text{O}$ or the composite sea level record (LR04 chronology)^{17,57}. However, in order to compare our AM record with marine IRD and benthic $\delta^{18}\text{O}$ records of ODP 980 and U1314 cores from the North Atlantic in Fig. 2, we have tuned their chronologies to our composite AM record through the correlation strategy as described in the main text: that is, by simple shifting of original chronologies to align the IRD events with WMIs as depicted by the grey bars in Fig. 2. In addition, we also tuned EDC ice core chronologies around the MIS 4/3 and 5.2/5.1 transitions in Fig. 2 by synchronizing the abrupt AM change with the CH₄ jump as described in the text. Amounts of age shifts from the original chronologies of the marine and ice core records are described in the figure legend.

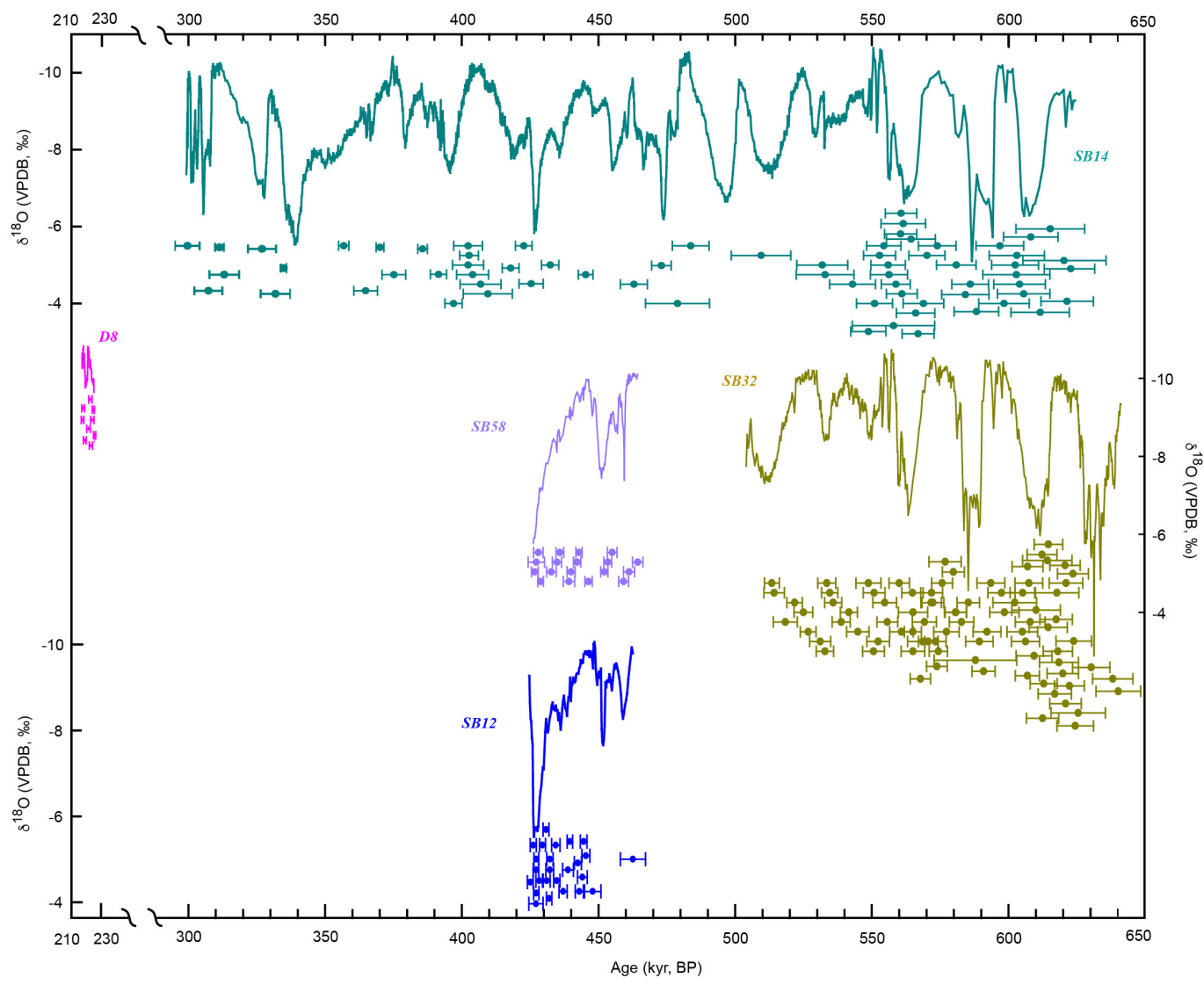
51. Edwards, R. L., Chen, J. H. & Wasserburg, G. J. ²³⁸U–²³⁴U–²³⁰Th–²³²Th systematics and the precise measurement of time over the past 500,000 years. *Earth Planet. Sci. Lett.* **81**, 175–192 (1987).
52. Cheng, H. *et al.* The half-lives of U-234 and Th-230. *Chem. Geol.* **169**, 17–33 (2000).
53. Spötl, C. & Vennemann, T. W. Continuous-flow isotope ratio mass spectrometric analysis of carbonate minerals. *Rapid Commun. Mass Spectrom.* **17**, 1004–1006 (2003).
54. Dykoski, C. A. *et al.* A high resolution, absolute-dated Holocene and deglacial Asian monsoon record from Dongge Cave, China. *Earth Planet. Sci. Lett.* **233**, 71–86 (2005).

55. Kelly, M. J. *et al.* High resolution characterization of the Asian Monsoon between 146,000 and 99,000 years B.P. from Dongge Cave, China. *Palaeogeogr. Palaeoclimatol. Palaeoecol.* **236**, 20–38 (2006).
56. Howell, P., Pisias, N., Ballance, J., Baughman, J. & Ochs, L. ARAND time-series analysis software (Brown Univ., 1997); available at <http://www.ncdc.noaa.gov/paleo/softlib/arand/arand.html>.
57. Lisiecki, L. E. & Raymo, M. E. A. Pliocene-Pleistocene stack of 57 globally distributed benthic $\delta^{18}\text{O}$ records. *Paleoceanography* **20**, PA1003 (2005).
58. Hendy, C. H. The isotope geochemistry of speleothems: I. The calculation of the effects of different modes of formation on the isotopic composition of speleothems and their applicability as paleoclimate indicators. *Geochim. Cosmochim. Acta* **35**, 801–824 (1971).
59. Lambert, F. *et al.* Dust-climate couplings over the past 800,000 years from the EPICA Dome C ice core. *Nature* **452**, 616–619 (2008).
60. Fleitmann, D. *et al.* Holocene forcing of the Indian monsoon recorded in a stalagmite from Southern Oman. *Science* **300**, 1737–1739 (2003).
61. Weldeab, S., Lea, D. W., Schneider, R. R. & Andersen, N. 155,000 years of West African monsoon and ocean thermal evolution. *Science* **316**, 1303–1307 (2007).
62. Holmgren, K. *et al.* Persistent millennial-scale climatic variability over the past 25,000 years in Southern Africa. *Quat. Sci. Rev.* **22**, 2311–2326 (2003).



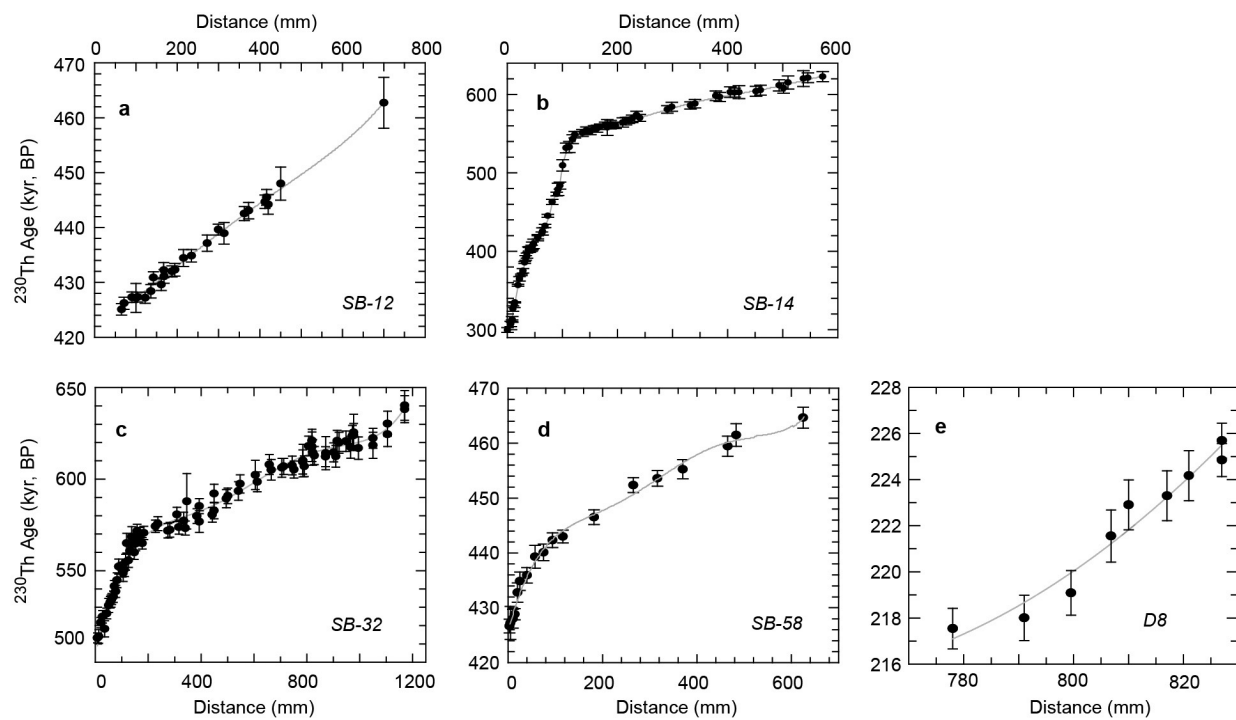
Extended Data Figure 1 | Schematic map of the vast Asian summer monsoon system. Arrows depict wind directions, yellow labels show wind names. The Mascarene High is a high pressure system near the Mascarene Islands. Stars indicate Sanbao ($31^{\circ} 40' N$, $110^{\circ} 26' E$), Hulu ($32^{\circ} 30' N$,

$119^{\circ} 10' E$) and Dongge ($25^{\circ} 17' N$, $108^{\circ} 5' E$) caves. The AM composite record is constructed from speleothem $\delta^{18}\text{O}$ records from these three caves. The map was constructed using NASA's World Wind program (<http://worldwind.arc.nasa.gov/java/>).



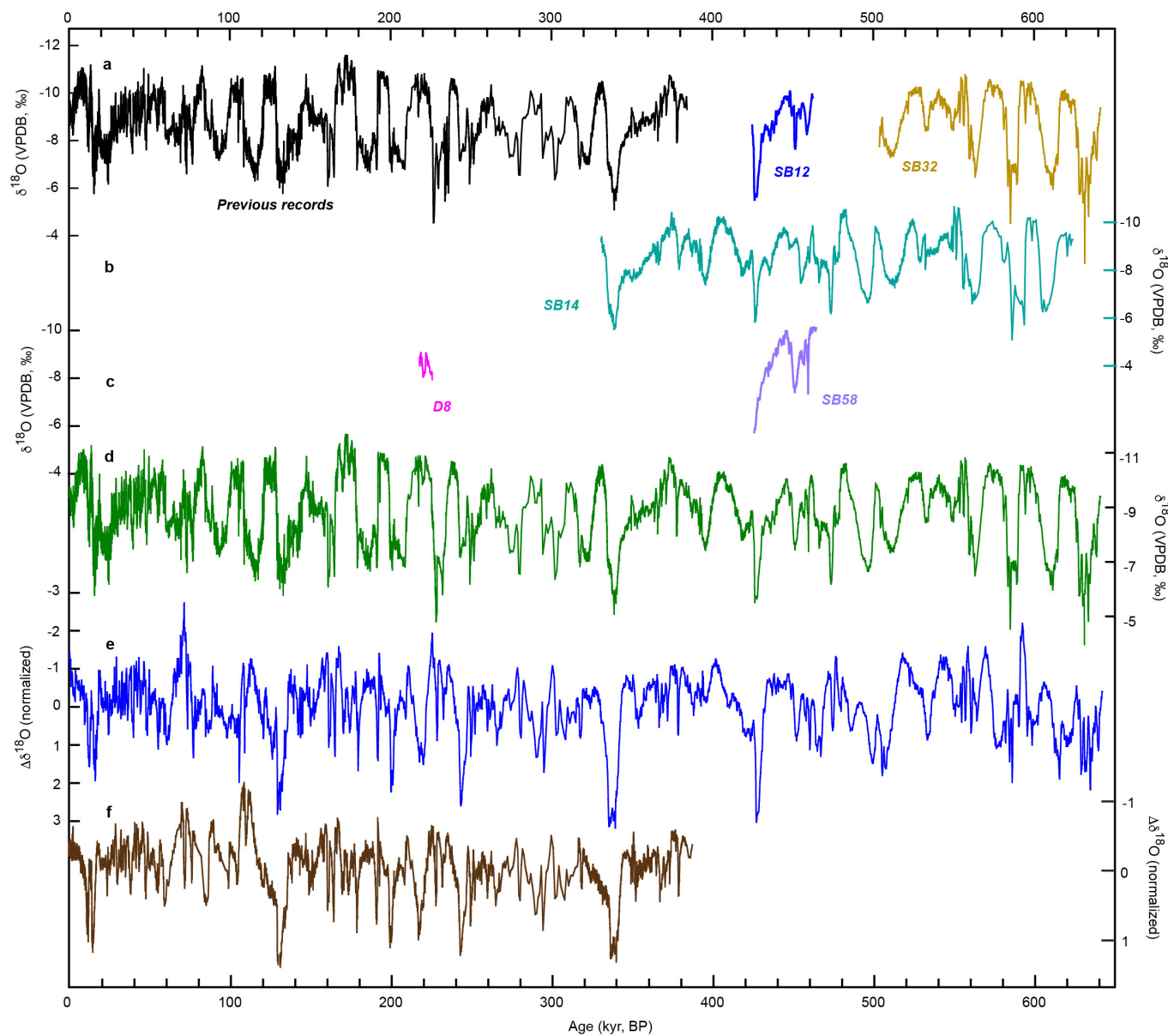
Extended Data Figure 2 | New speleothem records from China. Four new stalagmite $\delta^{18}\text{O}$ records used in this study are from Sanbao Cave, Hubei, China (labelled by sample numbers SB-12, SB-14, SB-32 and SB-58), and one is from Dongge Cave, Guizhou, China (labelled by sample number D8) (Fig. 1). Error bars indicate ^{230}Th ages and errors

(2σ). The ^{230}Th dating method is described in ref. 5 and the dating results are listed in Supplementary Table 1. A high degree of similarity among the coeval portions of different $\delta^{18}\text{O}$ records (the replication test^{2,58}) demonstrates that kinetic factors and water/rock interactions do not have a substantial effect on the speleothem $\delta^{18}\text{O}$ values.



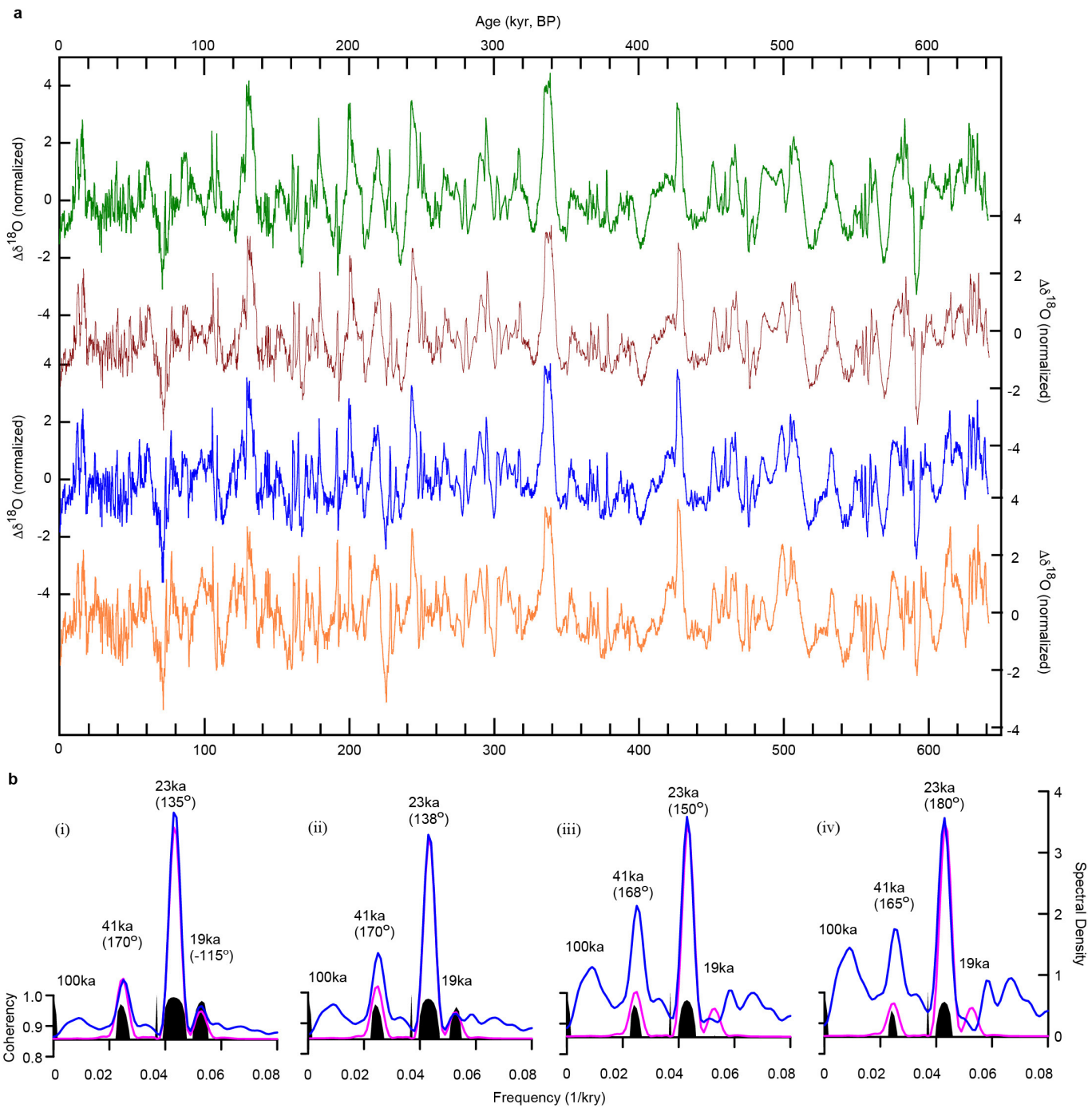
Extended Data Figure 3 | Stalagmite age models. a–e, Age models are shown for five stalagmites: SB-12 (a), SB-14 (b), SB-32 (c), SB-58 (d) from Sanbao Cave, and D8 (e) from Dongge Cave. The chronology of the upper part of SB-14 is established by linear interpolation between

successive ^{230}Th dates, whereas chronologies for other samples are based on polynomial fitting of ^{230}Th dates. The vertical error bars depict errors (2σ) of ^{230}Th dates.


Extended Data Figure 4 | AM records over the past 640 kyr BP.

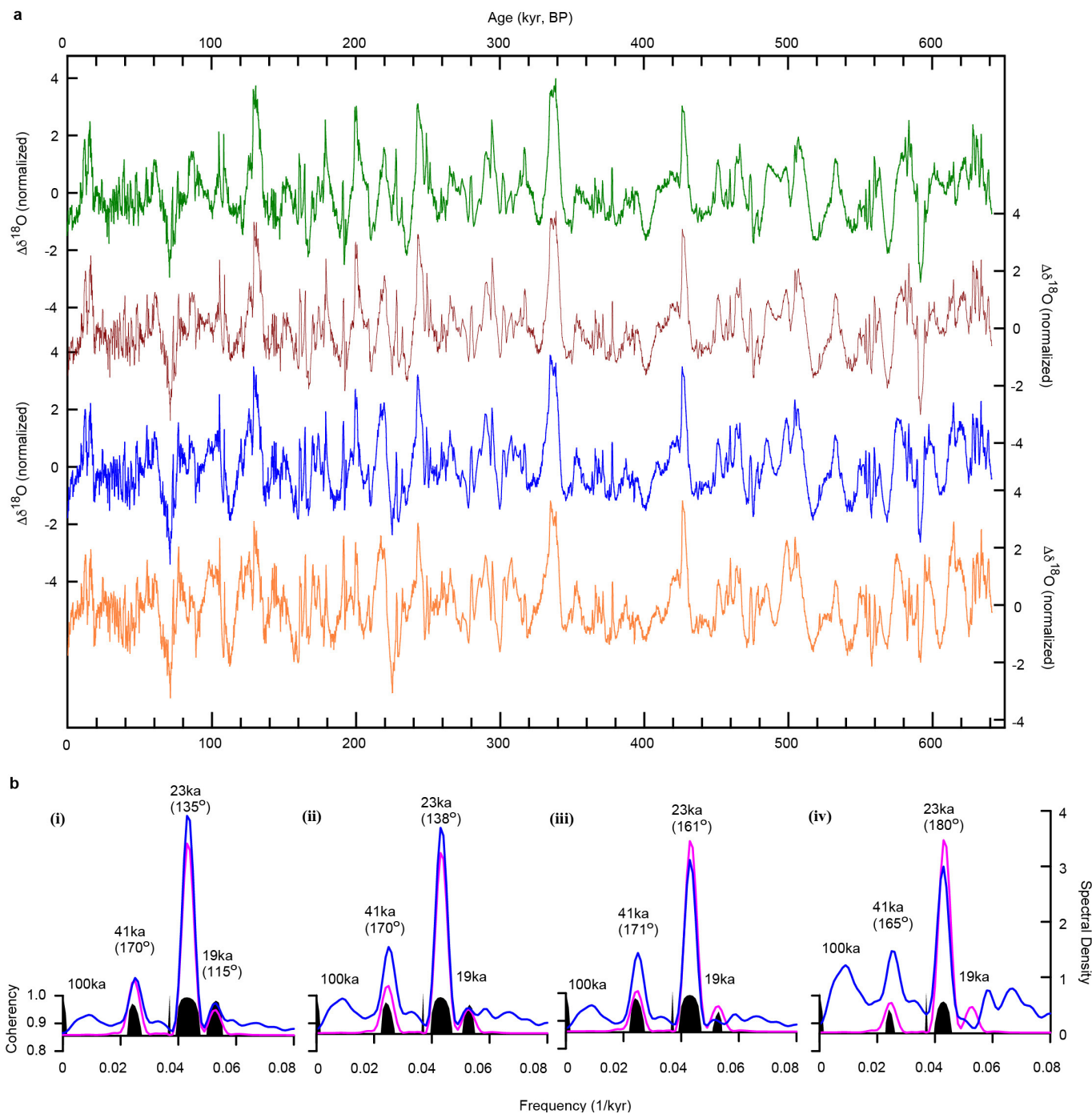
a, Previously published $\delta^{18}\text{O}$ records over the past 384 kyr BP (black) from Hulu, Dongge and Sanbao caves^{2–4,22,54,55}, and new SB-12 (blue) and SB-32 (olive) $\delta^{18}\text{O}$ records. b, New SB-14 $\delta^{18}\text{O}$ record. c, New SB-58 (purple) and D-8 (pink) $\delta^{18}\text{O}$ records. d, Composite AM $\delta^{18}\text{O}$ record over the past 640 kyr BP. The record is constructed from previous data (<384 kyr BP) and new data from four stalagmites from Sanbao Cave (≥ 384 kyr BP)

(see details in Methods and Supplementary Table 1). e, Detrended AM record ($\Delta\delta^{18}\text{O}$) is obtained by using the z-standard method to remove the insolation component (21 July insolation at 65° N) (see Methods). f, Detrended AM result from ref. 8, which is essentially identical to our results. Minor differences exist because the AM $\delta^{18}\text{O}$ records used in ref. 8 are slightly different.

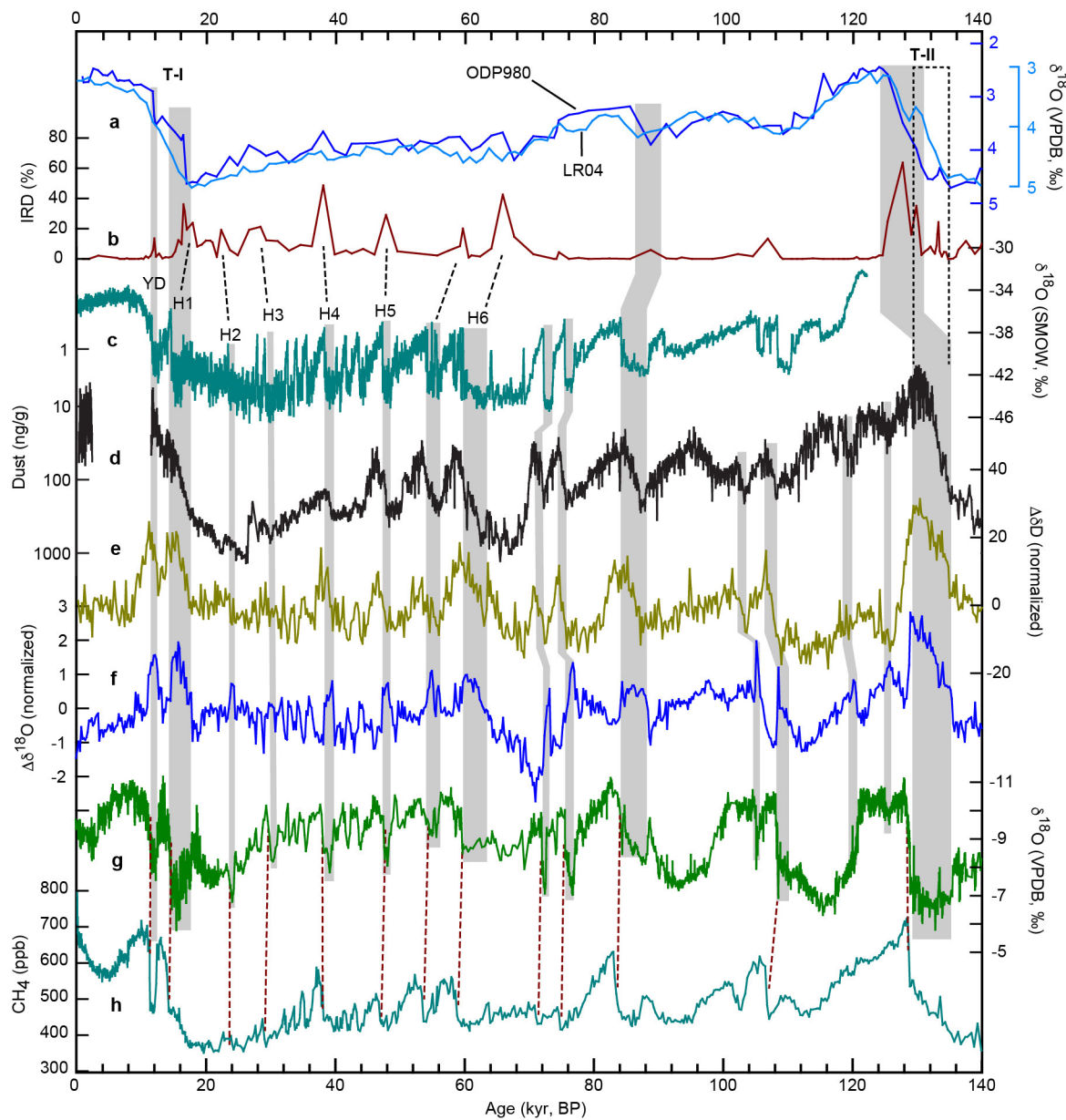


Extended Data Figure 5 | The AM $\Delta\delta^{18}\text{O}$ record over the past 640 kyr BP obtained by the z-standard method and cross-spectral comparison with insolation. **a**, Comparison among different AM $\Delta\delta^{18}\text{O}$ records detrended by subtracting 21 June (green), 6 July (brown), 21 July (blue) and 6 August (orange) insolation respectively, using the z-standard method (see Methods). **b**, Cross-spectral comparisons between the insolation for detrending (pink) and $\Delta\delta^{18}\text{O}$ records (blue) detrended by

21 June (i), 6 July (ii), 21 July (iii) and 6 August (iv) insolation respectively, using the z-standard method. Numbers in parentheses show the phase differences in degrees between insolation and $\Delta\delta^{18}\text{O}$ record. In all cases, the most significant power in the $\Delta\delta^{18}\text{O}$ record is in the precession band (~23 kyr). The ~41-kyr power is also present, but is relatively weak. The ~100-kyr power is insignificant.

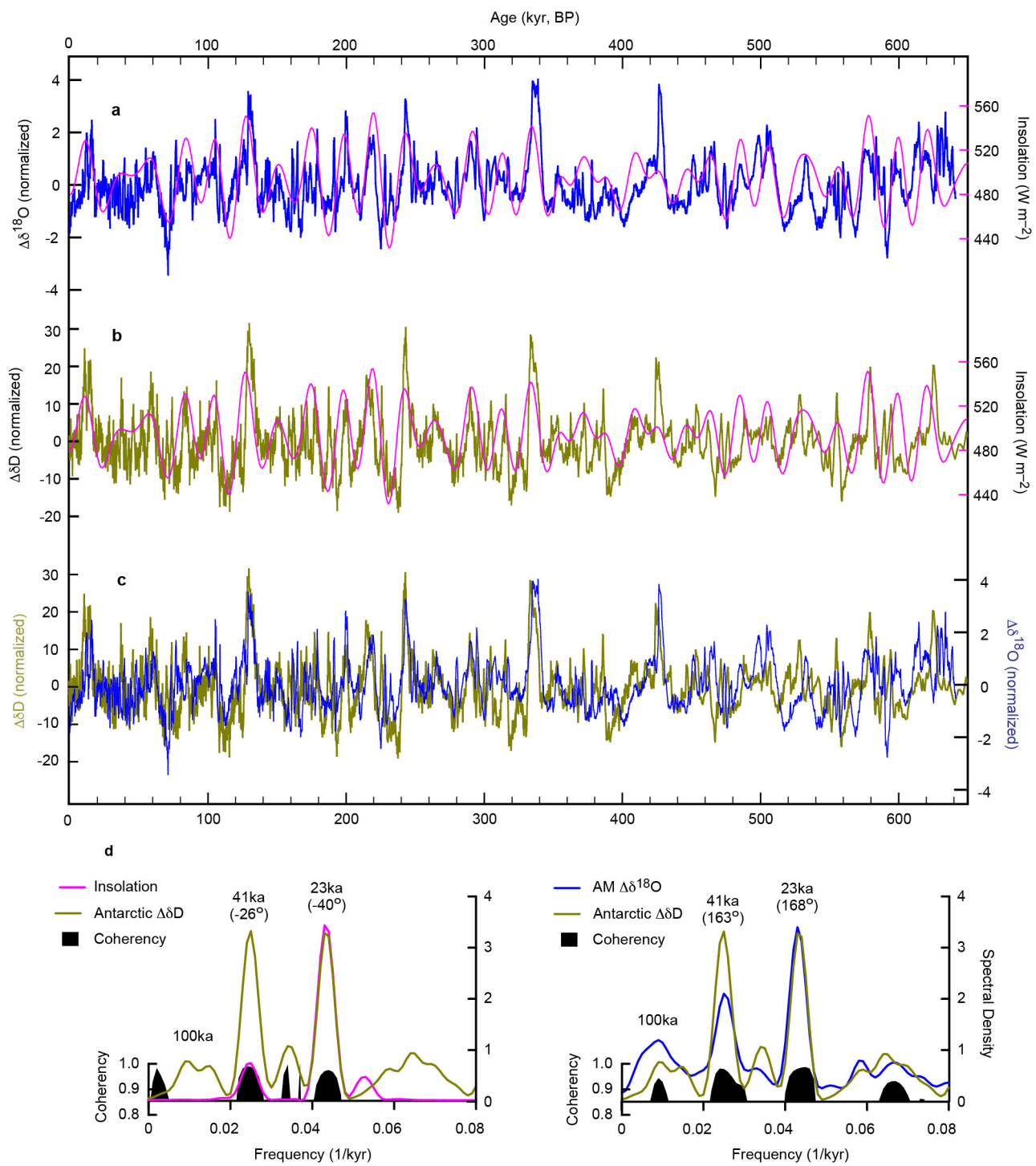


Extended Data Figure 6 | The AM $\Delta\delta^{18}\text{O}$ record over the past 640 kyr BP obtained by the principal component analysis method and cross-spectral analysis with insolation. **a, b,** As Extended Data Fig. 5, except the principal component analysis method was used, instead of the z-standard method.



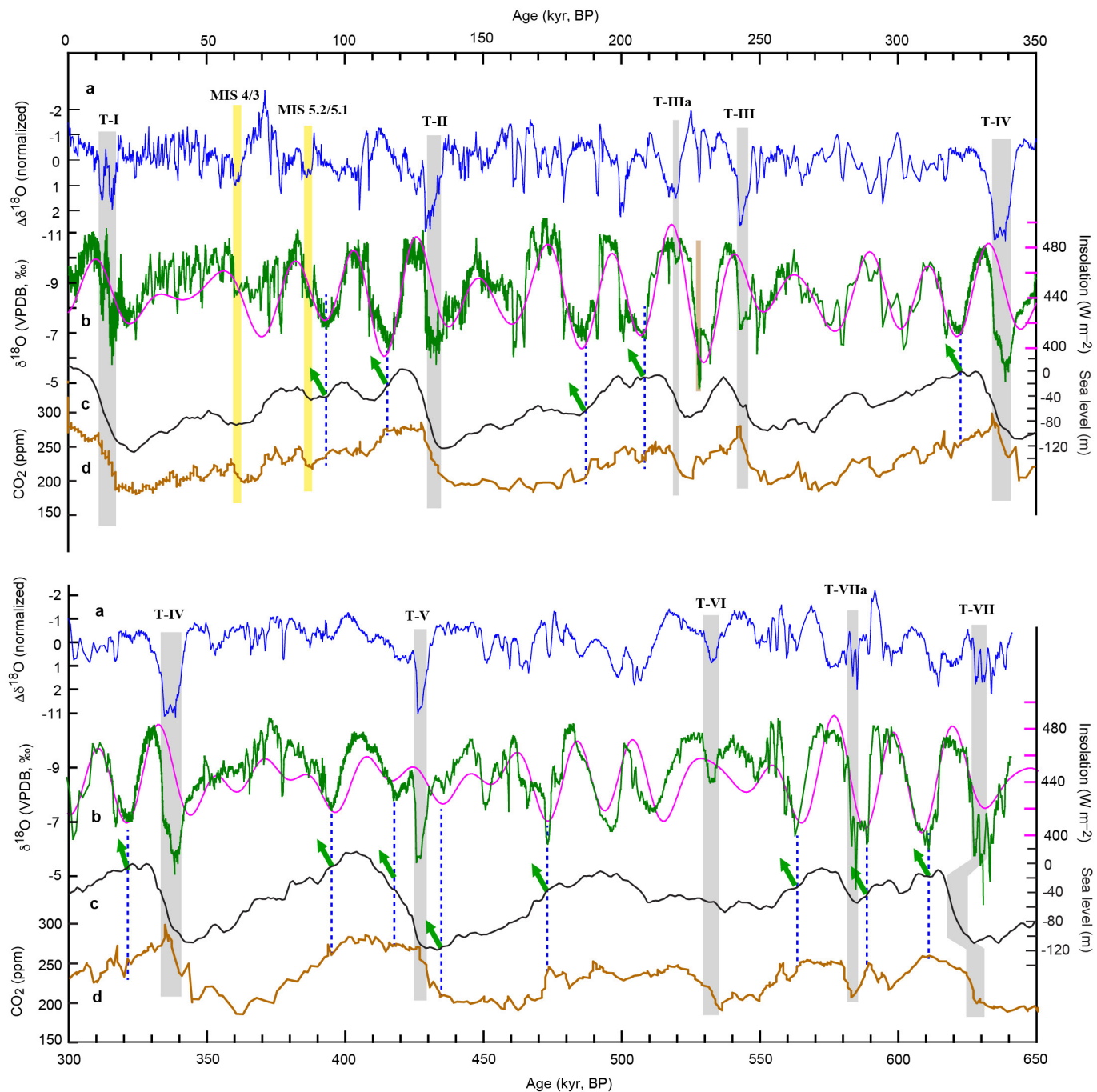
Extended Data Figure 7 | Comparison of millennial-scale climate events over the past 140 kyr. **a**, North Atlantic ODP980 (dark blue)⁷ and LR04 (light blue)⁵⁷ benthic $\delta^{18}\text{O}$ records. **b**, ODP980 IRD records⁷. We correlate the IRD event around T-II to the WMI with similar duration (depicted by grey bar), which is consistent with the obvious offset of its $\delta^{18}\text{O}$ shift related to that in LR04 record (dashed bar). YD and H1 to H6 indicate the Younger Dryas event, and Heinrich Stadial events 1 to 6, respectively. **c**, Greenland ice core (NGRIP) $\delta^{18}\text{O}$ record⁴⁹. **d**, Antarctic ice core (EDC) dust record⁵⁹. **e**, Detrended Antarctic $\Delta\delta\text{D}$ record¹⁸ ($\Delta\delta\text{D}$), using a method modified from ref. 35. **f**, AM millennial variability ($\Delta\delta^{18}\text{O}$, detrended

from the composite AM $\delta^{18}\text{O}$ record by subtracting 21 July insolation at 65° N). **g**, Composite AM $\delta^{18}\text{O}$ record. **h**, EDC CH₄ record¹⁹. Vertical grey bars indicate major weak AM intervals (WMIs) and corresponding events (increase of temperature and decrease of dust flux in Antarctica, cold events in Greenland and IRD events in the North Atlantic Ocean). Dashed lines depict correlations between abrupt AM intensification and CH₄ jump (brown) and between weak monsoon and IRD events (black). All ice core records are on their EDC3 chronology⁴⁶. Notably, the AM $\Delta\delta^{18}\text{O}$ and Antarctic $\Delta\delta\text{D}$ records show striking similarity, demonstrating a common millennial-scale variability (Fig. 3).



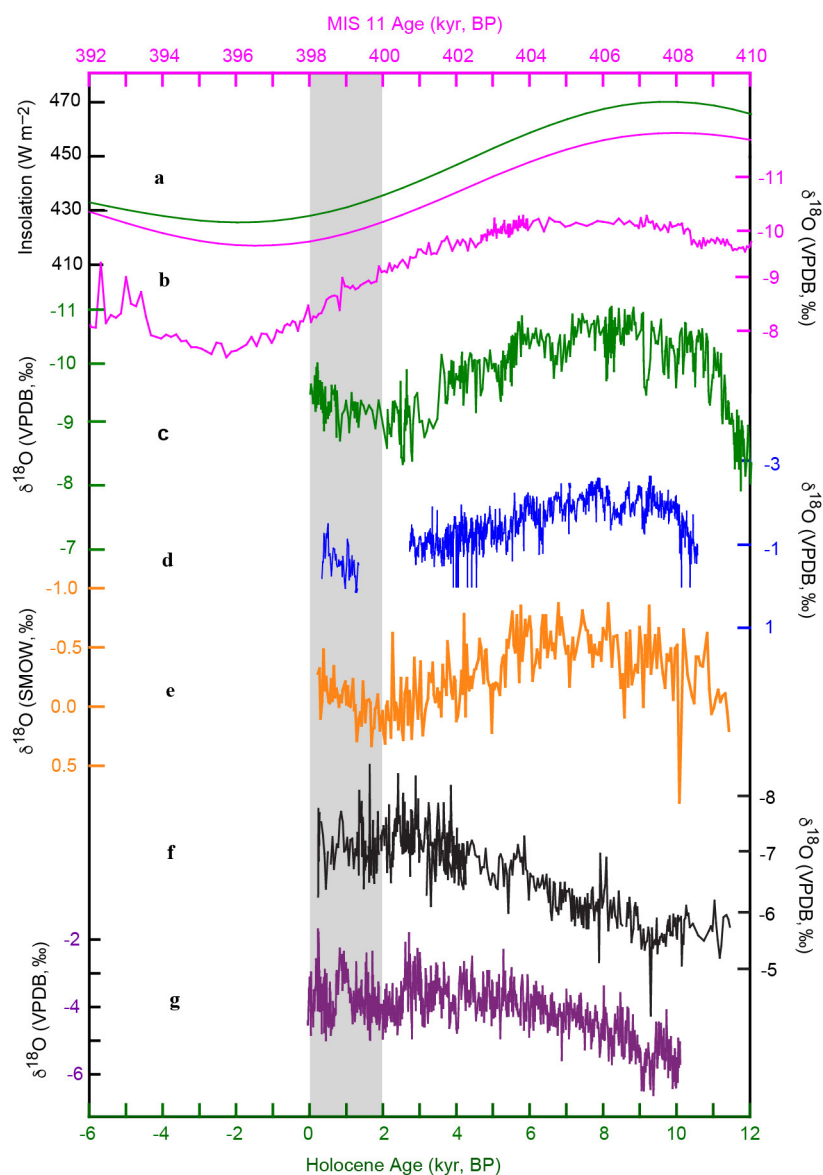
Extended Data Figure 8 | Comparison and cross-spectral analyses between insolation, AM $\Delta\delta^{18}\text{O}$ and Antarctic $\Delta\delta\text{D}$ records. **a**, AM $\Delta\delta^{18}\text{O}$ record (blue). **b**, Detrended Antarctic δD record¹⁸ ($\Delta\delta\text{D}$, olive), using a method modified from ref. 35. 21 June insolation at 65°N (ref. 45; pink) is plotted for comparison in **a** and **b**. **c**, Comparison between Antarctic $\Delta\delta\text{D}$ (olive) and AM $\Delta\delta^{18}\text{O}$ (blue) records. **d**, Cross-spectral analyses of the Antarctic $\Delta\delta\text{D}$ record (olive) with 21 July insolation at 65°N (pink)

(left), and with the AM $\Delta\delta^{18}\text{O}$ record (blue) (right), respectively. Numbers in parentheses show the phase differences in degrees. In all records, the precession cycle of ~ 23 kyr is significant. The phase of the Antarctic $\Delta\delta\text{D}$ record at precession band is close to 21 June insolation, and nearly anti-phased with the AM $\Delta\delta^{18}\text{O}$ record. The remarkable correlation between weak AM (positive $\Delta\delta^{18}\text{O}$ anomaly) and warm Antarctica (positive $\Delta\delta\text{D}$ anomaly) is evident (c).



Extended Data Figure 9 | Comparison of the AM variability with sea level (global ice volume) and atmospheric CO_2 changes. Upper panel, interval from 350 to 0 kyr BP; lower panel, interval from 650 to 300 kyr BP. In both panels: **a**, AM $\Delta\delta^{18}\text{O}$ record. **b**, AM $\delta^{18}\text{O}$ record (green) and 21 July insolation at 65°N (pink)⁴⁵. **c**, Composite sea level record¹⁷. **d**, Composite atmospheric CO_2 record²⁰. Grey bars show the timing of WMIs and associated terminations. Two yellow bars indicate the two millennial-scale positive anomalies (or WMIs), marking the ‘unfinished terminations’³⁰—the MIS 4/3 and 5.2/5.1 transitions (Fig. 2). For the

T-IIIa WMI we also indicate the correlation previously made by Cheng *et al.*⁴ with a beige bar. Although we consider this as a plausible alternative correlation, we prefer the new correlation presented in Figs 1, 3 and 5, and in this figure. The new correlation fits much better with the original chronologies of the ice core and marine records. In addition, the match of the adjacent high $\delta^{18}\text{O}$ AM anomalies and the ice rafted debris record⁷ is better with the new correlation. Some examples of initial AM rises around NHSI minima are depicted by green arrows and dashed lines, which do not appear to link directly to either global ice volume or CO_2 changes.



Extended Data Figure 10 | Comparison between the Holocene and MIS 11 on the basis of the insolation alignment. **a**, 21 July insolation at 65° N for the Holocene (green) and MIS 11 (pink)⁴⁵. **b, c**, Composite AM $\delta^{18}\text{O}$ records during MIS 11 and the Holocene, respectively. **d**, AM cave $\delta^{18}\text{O}$ record from the Indian monsoon domain⁶⁰. **e**, North African monsoon record (seawater $\delta^{18}\text{O}$ record from the marine sediment core, MD03-270, from the Gulf of Guinea)⁶¹. **f**, South American monsoon

record from Cueva del Tigre Perdido, northern Peru⁴⁰. **g**, South African monsoon record from Cold Air Cave, Makapansgat Valley, South Africa⁶². Vertical bar depicts the ‘2-kyr shift’. These records show ‘2-kyr shift’ trends that are different from their trends exhibited in the middle to late Holocene interval. The monsoon ‘2-kyr shift’ also appears to show an opposite inter-hemispheric pattern.